FORSCHUNGSZENTRUM JÜLICH GmbH

KFA

Institut für Festkörperforschung

Electronic and Geometric Structure of Buried $CoSi_2$ Layers investigated with Photon-in Photon-out Spectroscopies

Stefan Eisebitt

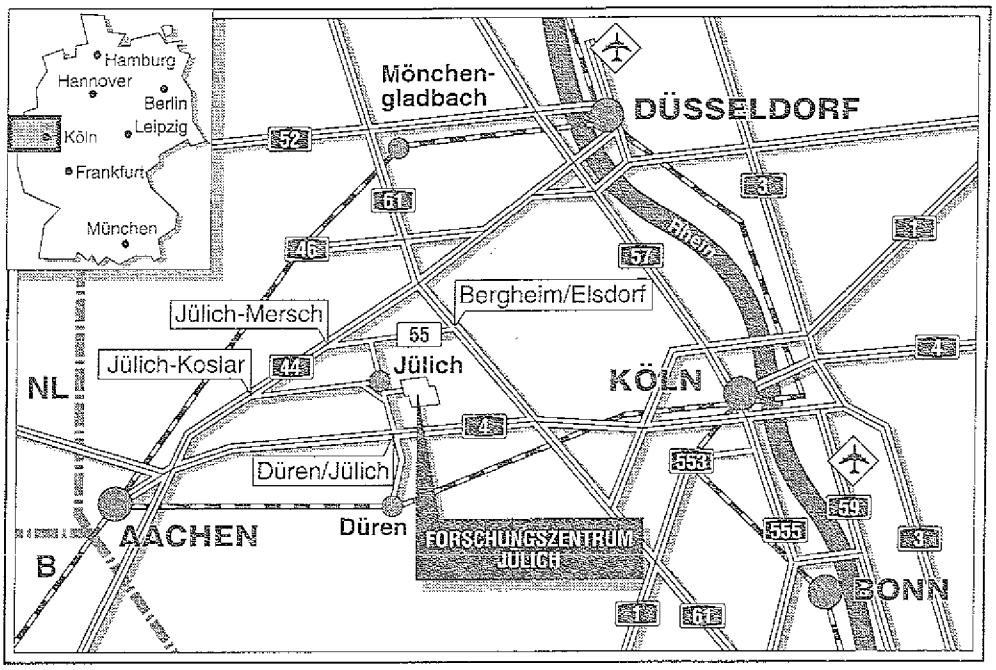

Berichte des Forschungszentrums Jülich ; 2715
ISSN 0366-0885
Institut für Festkörperforschung Jül-2715

Zu beziehen durch: Forschungszentrum Jülich GmbH · Zentralbibliothek
Postfach 1913 · D-5170 Jülich · Bundesrepublik Deutschland
Telefon: 02461/61-6102 · Telefax: 02461/61-6103 · Telex: 833556-70 kfa d

Electronic and Geometric Structure of Buried $CoSi_2$ Layers investigated with Photon-in Photon-out Spectroscopies

Stefan Eisebitt

Abstract

The electronic and geometric structure of $CoSi_2$ layers embedded in Si wafers by means of ion beam synthesis (IBS) has been studied. The work had two main directions: the development of methods suited to study buried structures in general and the actual investigation of the $CoSi_2$ layers.

In order to determine the geometric structure of buried silicides, we developed a method to use EXAFS at the $3d$ TM L-edges. We could demonstrate that this new technique is a promising alternative to K-EXAFS for samples in an environment of crystalline Si. The technique was established on a $CoSi_2$ IBS sample.

XANES detected by the fluorescence yield (FY) is another technique suited to study buried structures *in situ* due to its deep-probing character and its atomic selectivity. The saturation effects in FY spectra of concentrated samples were analysed. Using the dependence of the FY intensity on the geometry of the experiment, we developed a new method to calculate the absorption coefficient from spectra recorded at different angles. The information depth of the technique has been investigated.

We applied this method to the Co L_3 near-edge absorption in order to investigate the unoccupied electronic states of buried $CoSi_2$ layers by FY-XANES. Additionally, the occupied electronic states of these structures produced by IBS were studied by soft x-ray emission (SXE) spectroscopy. As a result, we obtained a complete picture of the Co d-DOS with a resolution that allowed for a detailed comparison to theoretical calculations.

By investigating a $CoSi_2$ single crystal in addition to an as-implanted and an annealed IBS sample we gained insight into the evolution of the electronic structure upon silicide formation in the IBS process. We could proove that single crystalline $CoSi_2$ is indeed formed upon annealing.

The results show that the experimental methods applied can be used for non-destructive investigations of buried layers in microelectronic devices.

Publications related to this work:

Electronic Structure Determination of Ion Beam Synthesized $CoSi_2$ using Photon-in Photon-out Spectroscopies
S. Eisebitt, T. Böske, J.-E. Rubensson, R. Jebasinski, S. Mantl, J. Kojnok, P. Skytt, J.-H. Guo, N. Wassdahl, J. Nordgren, K. Holldack, and W. Eberhardt, submitted to Phys. Rev. B.

Determination Of Absorption Coefficients For Concentrated Samples By Fluorescence Detection
S. Eisebitt, T. Böske, J-E. Rubensson and W. Eberhardt, submitted to Phys. Rev. B.

Contents

Abbreviations

ASW	Augmented Spherical Wave
DOS	Density Of States
EELS	Electron Energy Loss Spectroscopy
EXAFS	Extended X-ray Absorption Fine Structure
EY	Electron Yield
FLAPW	Full Potential Linearized Augmented Plane Wave
FY	Fluorescence Yield
IBS	Ion Beam Synthesis
LPDOS	Local Partial Density Of States
MBT	Metal Base Transistor
NEXAFS	Near Edge X-ray Absorption Fine Structure
PBT	Permeable Base Transistor
RBS	Rutherford Backscattering
SXA	Soft X-ray Absorption
SXE	Soft X-ray Emission
TM	Transition Metal
XANES	X-ray Absorption Near Edge Fine Structure
XPS	X-ray Photoelectron Spectroscopy
XTEM	Cross-sectional Transmission Electron Microscopy

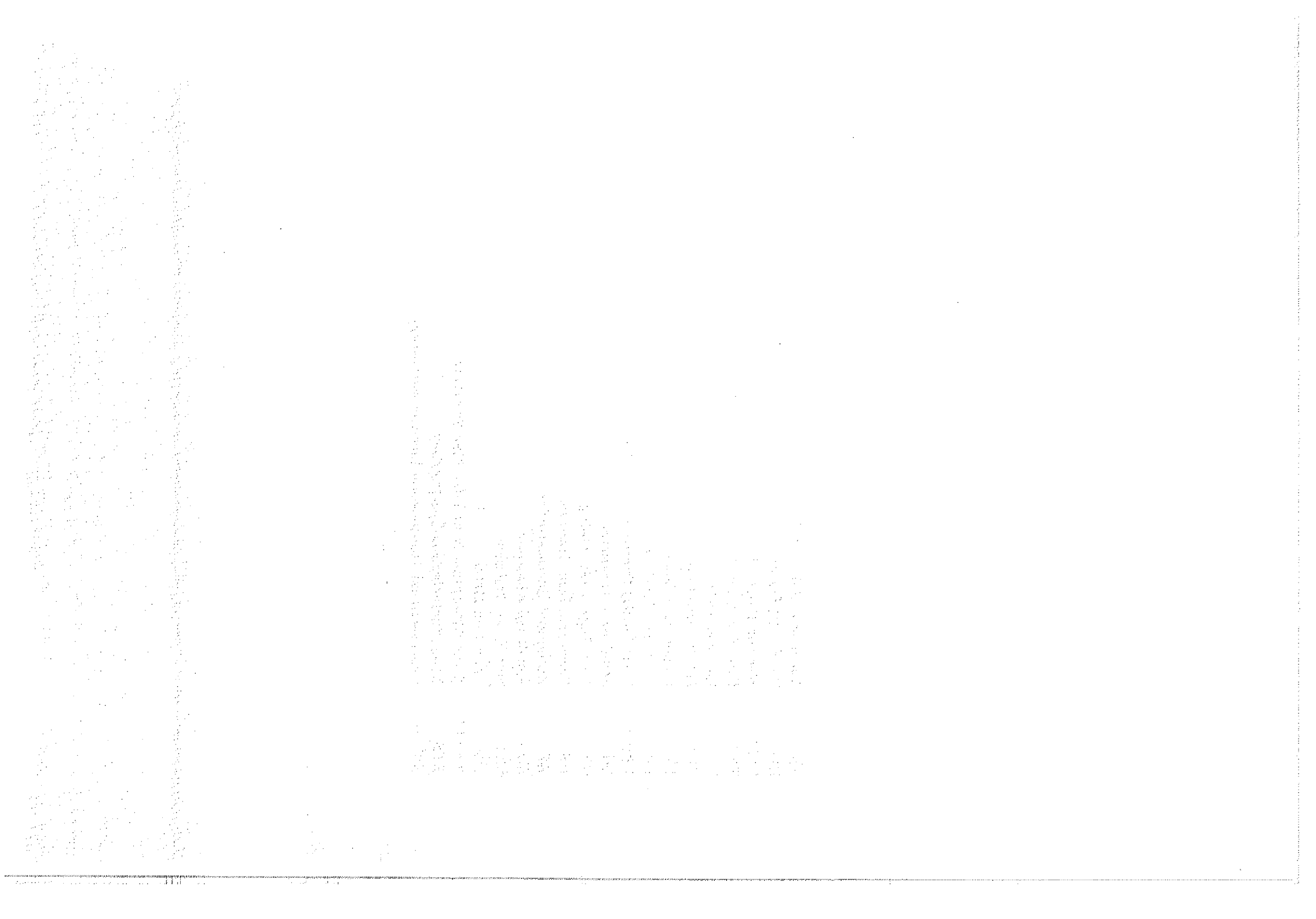

1 Introduction

There have been numerous studies of transition metal silicides over the last decade. Especially $CoSi_2$ has attracted much interest because it can be grown epitaxial on Si, due to the small lattice mismatch. The low specific resistivity of $CoSi_2$ makes it suitable for special microelectronic devices such as metal-base (MBT) and permeable base (PBT) transistors [1, 2, 3] (See Fig. 1). Ion beam synthesis (IBS) has overcome growth problems of epitaxial $CoSi_2$ on Si(100) encountered by conventional deposition techniques [4]. With IBS well-defined buried layers of transition metal disilicides with sharp interfaces to a Si substrate can be formed [5] and first PBTs have already been successfully fabricated [6].

To investigate the electronic structure of $CoSi_2$ is thus not only of basic scientific interest in solid state research. As the valence electronic structure determines the conductivity and other electronic properties of a given material, this investigations are of importance for the development of microelectronic devices which rely upon the electronic properties of their components.

In order to understand the electronic structure it is desirable to determine the geometric structure as well, since electronic and geometric structure influence each other. The valence electronic structure constitutes the chemical bonding and is hence coupled to the atomic topology of the sample. In addition, the geometric structure yields information about the quality of the layer produced. This is important information in order to optimize the IBS production process.

The electronic and geometric structure of such buried structures can not be studied using conventional electron spectroscopies. The short electron mean free path even for inellastically scattered electrons makes it impossible to carry information from the buried layer through a silicon cap layer of several hundred Ångström thickness. One can, however, take advantage of the larger photon penetration length, and use spectroscopies where photons carry the physical information.

We have studied the electronic structure of $CoSi_2$ layers buried in Si by means of IBS [7] using Fluorescence Yield Soft X-ray Absorption (FY-SXA) and Soft X-ray Emission (SXE) spectroscopy [8]. Results are presented in section 5. The atomic selectivity of the x-ray processes and the large information depth makes these techniques ideal to study buried structures.

In order to monitor the X-ray Absorption Near Edge Structure (XANES) for concentrated samples by FY detection, we developed a new method to calculate the absorption coefficient from spectra recorded at different angles [9]. This method is established in section 4.2.

The analysis of the Extended X-ray Absorption Fine Structure (EXAFS) is a powerful tool for determination of the local geometric structure. However, it is difficult to combine conventional EXAFS spectroscopy at the 3d transition metal (TM) K-edges with the FY detection mode needed to investigate buried structures if the TM is located in a crystalline environment. In section 4.1 we demonstrate that it is possible to extract geometrical information from the EXAFS recorded at the Co L-edges in a buried $CoSi_2$ layer. As L-EXAFS is compatible with the FY detection mode, this is a promising new tool for the investigation of buried structures.

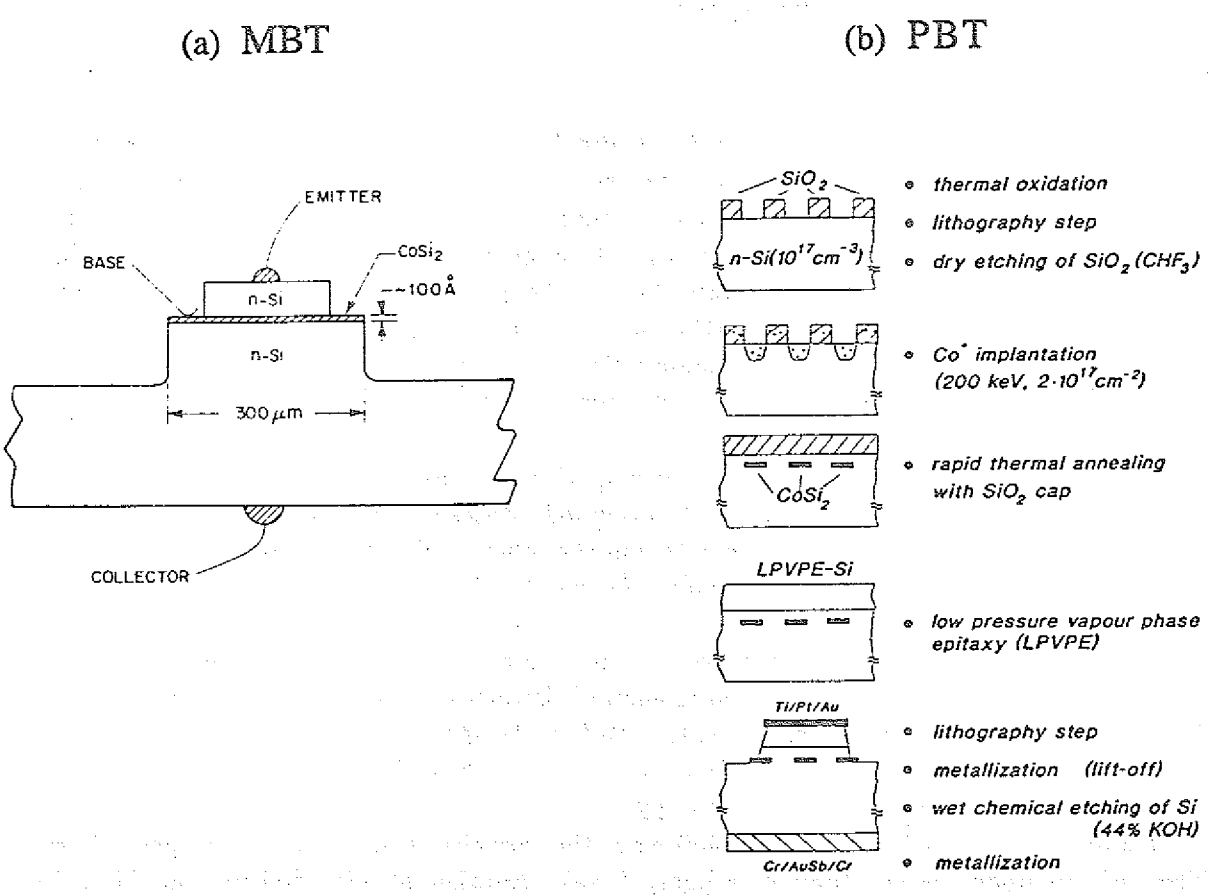

Figure 1: Applications of buried $CoSi_2$ structures in microelectronics. (a) Metal Base Transistor (MBT) [1], (b) fabrication steps for a Permeable Base Transistor (PBT) [5].

2 Experimental Techniques

2.1 Introduction

In the early days of modern physics, x-ray transitions have been used to study the electronic structure of atoms and molecules. Measuring the wavelength of the absorbed radiation in x-ray absorption or of the emitted radiation in x-ray emission, the atomic energy levels were mapped.

When many atoms are close to each other forming a solid, the deep core levels are nearly unaffected by the chemical bonding. Only slight shifts in the energy position occur. The valence electron levels, however, are strongly affected. They form energy bands which are occupied by electrons up to the Fermi level and are unoccupied above. Most physical properties of a material can be derived from the structure of these electronic bands and their investigation is a main task in solid state physics.

Again, x-ray transitions can be used to map these energy bands to obtain insight into the electronic structure. Information about the occupieds states can be extracted by analysing transitions from the valence band to a core hole. On the other hand, spectroscopy of transitions from a core level to the conduction band yields information about the unoccupied electronic energy levels.

As far as the x-ray emission is concerned, it is important to use core levels of low binding energy as the lifetime broadening at high energies becomes so large that no information about the valence electronic structure can be extracted fom the spectra. In addition, no disturbing core to core transitions are present. Thus it is necessary to study the emission of low energy x-rays using soft x-ray emission (SXE) spectroscopy.

Traditionally one refers to x-rays as soft when they are absorbed by air of atmospheric pressure. This sets an upper energy limit of roughly 5 keV. Another natural division can be made on technical grounds. In the energy range between 30 and 1000 eV reflection gratings in grazing incidence have to be used to monochromatize the radiation. X-rays in this sub-keV range are sometimes named "ultra-soft". However, as the literature is not unambiguous on that point we will refer to these x-rays as "soft" in the following.

It is obvious that soft x-ray absorption (SXA) spectra contain information about the unoccupied electronic states only if the electron is transferred into unoccupied valence states. This happens if the energy of the exciting photon is only slightly above the absorption edge. Hence the x-ray absorption near edge structure (XANES) has to be analysed. If the energy in an x-ray absorption process is sufficiently high, the electron is transferred into states where it can be described as nearly free. Spectra recorded in this higher energy range exhibit an extended x-ray absorption fine structure (EXAFS). This structure is mainly due to single scattering contributions from neighbouring atoms to the outgoing electron wave. Thus EXAFS spectra contain information about the local *geometric* structure of the sample.

EXAFS and XANES represent two extreme cases of SXA spectroscopy. The EXAFS description is valid in the high energy range, where the electon is nearly free and can be described by plane wave wavefunctions. In this limit, a short range single scattering theory is the most appropriate description for the process. On the other hand, we are in the low energy limit for

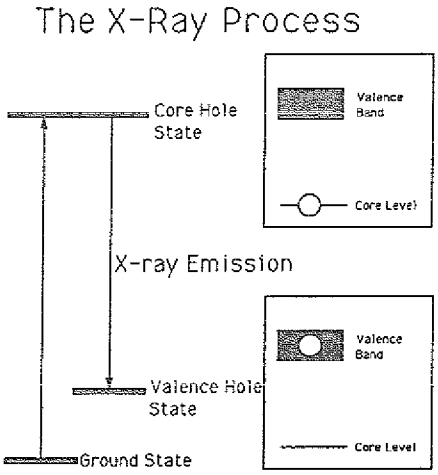

Figure 2: The X-ray process. (From [10])

the ejected photoelectron in the XANES energy range. Here the spectra are most successfuly described in terms of the unoccupied Density Of States (DOS). However, we would like to stress the point that no sharp line can be drawn between the two descriptions. XANES can be described in a scattering picture, if multiple scattering is taken into account. On the other hand, EXAFS can be understood as a modulation of the DOS for the nearly free electron due to the local arrangement of atoms around the central atom which lost the electron.

In this method section we present how SXE and and XANES spectra can be interpreted in terms of the electronic structure of solids. Furthermore we present the basic theory needed to extract information about the geometric structure from EXAFS spectra.

2.2 Electronic structure

2.2.1 Interpretation of SXE and XANES spectra in terms of the local partial density of states

SXE occurs when a core vacancy is filled by a valence electron. Thus the initial state $|i>$ for the SXE process is an excited state with a core hole, while the final state $<f|$ contains a valence hole as shown in Fig. 2. The energy of the photon produced is the energy difference between the initial and the final state: $h\nu = E_i - E_f$. This energy is equal to the difference of the core and valence electron binding energies ϵ_c and ϵ_v. As the atomic dimensions are small compared to the wavelength in the the SXE region, Fermi's golden rule for the transition probability $\omega_{i\to f}$ can be applied in the dipole approximation:

$$\omega_{i\to f} \propto |<f|\hat{r}|i>|^2 \, \delta(E_i - E_f - h\nu) \quad , \tag{1}$$

where $\hat{r}$ denotes the dipole operator.

If the initial and final state wavefunctions can be factorized into single electron wavefunctions $|i_c>$ and $<f_v|$, a simple one-electron picture as sketched in Fig. 3 can be used to describe the

process [1]. Using usual [2] core wavefunctions and Bloch wavefunctions expanded in atomic-like functions around the atom of interest [11, 12], the angular integration results in the selection rules

$$\Delta l = \pm 1 \quad , \tag{2}$$

$$\Delta m = \pm 1 \quad \text{or} \quad 0 \quad , \tag{3}$$

and after adding over all possible final states in the following expressions for the x-ray intensities [13].

From an initial 1s core hole only final states of p symmetry can be reached:

$$I_s(E_{emit}) \propto E_{emit}^3 \, N_p(E) \, M_{s,p}^2(E) \quad . \tag{4}$$

From an initial 2p core hole transitions to s and d final states are possible:

$$I_p(E_{emit}) \propto E_{emit}^3 \, [N_s(E) M_{p,s}^2(E) + \frac{2}{5} N_d(E) M_{p,d}^2(E)] \quad . \tag{5}$$

Here $E_{emit} = h\nu$ denotes the energy of the emitted photon while E is the binding energy of the valence electrons refered to the Fermi level. They are connected by $E = E_{emit} - \epsilon_c$ if the core electron binding energy ϵ_c is referred to the Fermi level as well. N denotes the occupied density of states (DOS) of the indicated symmetry type. The terms $M_{x,y}(E)$ refer to the radial matrix elements for the transition in question. As they contain the highly localized radial function of the initial core hole state, they are only nonzero in the vicinity of the atom involved in the transition.

Under the simplifying assumptions made, eqns. (4) and (5) can be expressed in this rule:

SXE probes the occupied local partial density of states (LPDOS).

We now will discuss the implications of this rule for the determination of the electronic structure by SXE spectroscopy in further detail.

1. SXE probes the occupied *DOS*

Looking at Fig. 3 it seems obvious that the transition rate and thus the SXE intensity is proportional to the density of initial states, thus mapping the valence band DOS. Nevertheless, from eqns. (4) and (5) it is clear that the energy variation of the matrix elements has to be taken into account. Thus it is important to check this point with matrix element calculations. However, in most cases it turns out that the variation of the matrix elements over the narrow energy range of interest is smooth and small compared to the changes in the DOS. In these cases SXE directly maps the occupied DOS.

[1] Using single-electron wavefunctions implicates that correlation between the electrons is not important. Correlation effects will be discussed in the next section in more detail.

[2] How the core hole in the initial state is taken into account will be discussed in the context of the final state rule (next section).

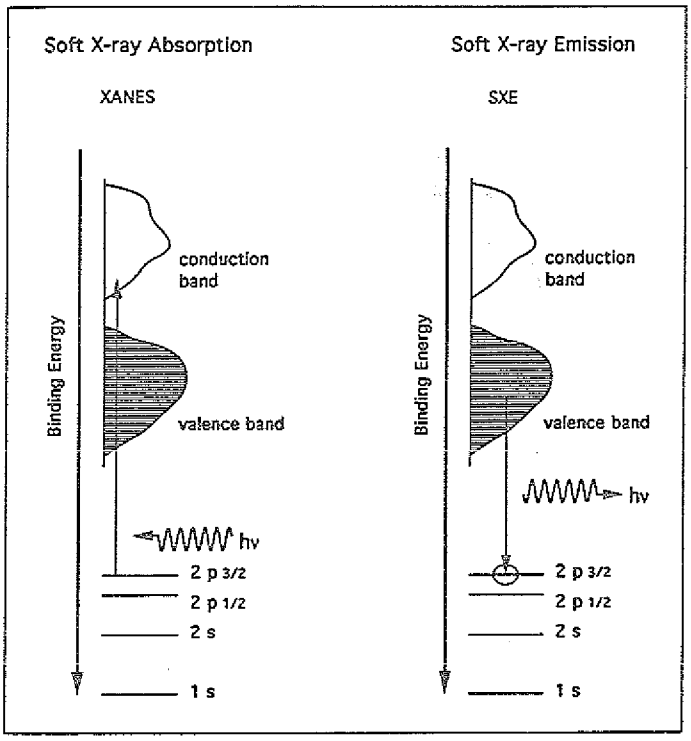

Figure 3: Schematic picture of the SXE and SXA processes.

2. SXE probes the *partial* DOS

A direct consequence of the dipole approximation, which is clearly justified in the soft x-ray energy range, is the angular momentum selection rule in eqn. (2). Since valence band Bloch functions must have translational symmetry, angular momentum is not a good quantum number for the Bloch functions. Thus it is at a first glance surprising that this selection rule is of importance for transitions involving the valence band. However, the Bloch functions can be expanded in atomic-like functions locally around a specific atom. This is why the angular momentum is locally well- defined in the valence band too.

Consequently, SXE spectroscopy is able to resolve components of the DOS belonging to different angular momentum symmetries: the partial DOS is mapped. If an s-type core hole is chosen as initial state, SXE monitors the p DOS as described in eqn. (4). If a vacancy in a p core level is produced by the experimentator, SXE will map a superposition of s- and p-type DOS (eqn. (5)).

3. SXE probes the *local* DOS

The initial state of the SXE process is a core hole state. Such states are strongly localized in the vicinity of the nucleus of the atom in question. The SXE intensity depends on the overlap of this core orbital with the valence Bloch functions as given by the radial matrix elements for the transition. Thus SXE spectroscopy maps the DOS only in the vicinity of the atom, in which the initial core hole was produced. The "information radius" for SXE is normally on the order of one atomic distance [10].

The merits of this atomic selectivity are illustrated in Fig. 4. Assume that the elements A and B with their unique electronic structure form a compound AB in a chemical reaction. As the core

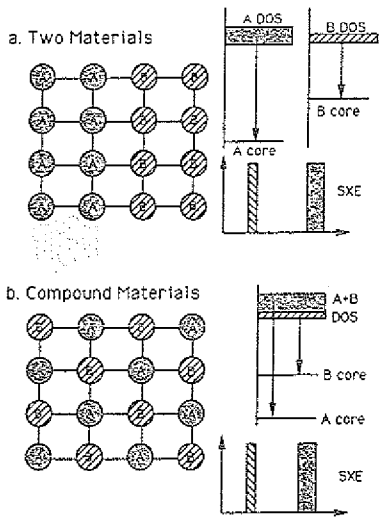

Figure 4: SXE probes the *local* DOS. See text for details. (From [10])

level of the elements A and B are usually different in energy, they might be excited selectively to study the new electronic structure of the compound AB. Due to the short information radius, the electronic structure in the vicinity of an B atom is monitored specifically by SXE if a B core hole is produced in the excitation. Even if atoms A and B are both excited in the experiment, their SXE can be analyzed separatly as their x-ray emission falls at different energies in the spectrum due to the different core electron binding energies.

In a compound one can thus study the contributon of the various atoms to the chemical bonding and the local electronic structure in general. Another advantage of the locality is the possibility to investigate buried layers and the electronic surrounding of atoms that make up only a very small fraction of the atoms in the material, *e.g.* dopants.

As the core hole binding energy ϵ_c determines the energy position of the SXE, it can be determined in SXE spectroscopy, if the Fermi energy can be localized in the spectrum. Thus SXE contains information about core level shifts in addition to the valence band LPDOS, too.

In a XANES experiment the photoabsorption coefficient μ is monitored at and close above an absorption edge by varying the energy of the incoming photons. As the energy of the exciting photon is only slightly higher than the core electron binding energy, the core electron will be transferred into an unoccupied valence state[3] of the sample. Thus the final state $< f|$ for the transition contains a core hole and an additional electron in the valence band, while the initial state $|i >$ is the ground state of the electronic system, where no excitations are present. The

[3]This description assumes the bandstructure of a metal. If the sample is semiconducting, the first unoccupied valence states are situated in the conduction band. We will continue using the terminology for the metallic case, implicitly assuming the validity of the statements for the semiconducting case as well.

theoretical description of the process is basically parallel to the description for the SXE process. The XANES process is shown diagramatically in a single-electron picture in Fig. 3.

Making the same assumptions as in the SXE case, the XANES spectrum can be interpreted in terms of the density of unoccupied electronic states. For the same reasons as discussed above in the context of SXE, the *local partial DOS* is measured in the experiment:

XANES probes the unoccupied local partial density of states.

For K absorption edges, the absorption coefficient can be written as

$$\mu_K(E_{abs}) \propto N_p(E) M^2_{s,p}(E) \quad . \tag{6}$$

For L absorption edges, the equation

$$\mu_L(E_{abs}) \propto [N_s(E) M^2_{p,s}(E) + \frac{2}{5} N_d(E) M^2_{p,d}(E)] \tag{7}$$

is derived. E_{abs} denotes the energy of the absorbed photons while E is refered to the Fermi level by $E = E_{abs} - \epsilon_c$. In this context N describes the *unoccupied* DOS of the symmetry type indicated, while $M_{x,y}(E)$ refers to the radial matrix element for the transition in question. The equations are analog to the eqns. 4 and 5, though there N denoted the *occupied* DOS. Another difference is the E^3_{emit} factor in SXE, which is caused by the degrees of freedom for the emitted photons[4]. Like in the case of SXE, core level shifts can be detected in XANES if the energy position of the Fermi edge can be determined from spectral features[5]. Nevertheless, in spite of the obvious similarities in SXE and XANES, one has to be aware of the presence of the core hole in XANES. This will be discussed in the context of the *final state rule* in the next section.

2.2.2 Dynamical effects in SXE and XANES

To derive the simple intensity relations (4), (5), (6) and (7) we avoided some complications which are related to dynamical effects of the excitation process or of the SXE or XANES process itself. The dynamical effects most important for both types of spectroscopy are discussed in this section.

The final state rule. In the previos section we claimed that the intensity of the SXE is connected to the LPDOS. However, a core hole excitation is a huge distortion of an electronic system. The additional charge at the core produces a different potential resulting in new system of eigenstates. Relaxing into the new ground state, the electronic structure of the valence band will be affected. After the x-ray emission, the core vacancy is filled by a valence electron, leaving a valence hole behind. So the question arises: *Which* DOS will be measured? Is it the DOS of the excited system containing the core hole or the DOS of the system without the core vacancy? In other words: Is the SXE spectrum determined by the initial or the final state of the system? This question has been discussed controversially in the past, not only with respect to SXE but

[4]The same physics is reflected in the fact that the Einstein coefficients for absorption and spontaneous emission are connected by this energy factor, too.

[5]The identification can be difficult if the presence of core excitons distorts the spectra at the absorption threshold.

also for SXA. Here, the final state contains a core hole and an additional electron in the valence band which are both not present in the initial state.

At the present time it is generally assumed that the final state is determining the SXE and SXA spectra, at least for simple metals. Though there is no strict theoretical proof for the so-called *final state rule*, it has been derived approximately by von Barth and Grossman [14] and it has vast experimental support.

Consequently, SXE measures the ground state LPDOS without a core hole present while the LPDOS as derived by XANES is influenced by the presence of the additional charge.

Satellites. The satellite concept refers to the fact that SXE spectra sometimes contain intensity which is not related to transitions between pure single-hole states as discussed before. The structures produced are called satellites and are due to transitions between states which contain additional excitations. They can be divided into initial state satellites and final state satellites.

Final state satellites in SXE are caused by transitions of the type $|i> \rightarrow < f^*|$, where the final state contains an additional excitation. This additional excitation is created in the SXE process. The most common additional excitations are plasmons and excitons. As the energy E_{f^*} of the excited final state is higher than the energy E_f of the final state associated with the main transition, final state satellites always fall on the low energy side of the main emission line. A similar process can be imagined in XANES as well. A fraction of the energy of the absorbed photon can be used to create an additional excitation in the final state.

Initial state satellites are produced in SXE transitions $|i^*> \rightarrow < f^*|$ where an additional excitation is present in the inital state. This extra excitation is usually a core hole and/or a valence exciton, created by excess energy while producing a core vacancy. They affect the SXE spectrum due to Coulomb interaction. The energetics of initial state satellites is shown in the total energy diagram in Fig. 5. On which side of the main transition the initial state satellites fall, depends on the magnitude of the different Coulomb interactions involved. Double core hole satellites always fall on the high energy side, as the interaction of the two core holes $U_{c,c}$ in the initial state is much larger than the interaction $U_{c,v}$ between the core and valence hole in the final state. Thus they are usually well-separated from the main emission. Spectral features due to an additional valence hole are termed double hole satellites. Their apperarance depends critically on the valence band width. If the band width is large compared to the lifetime width of the core hole, the initial state valence hole will be able to delocalize before the SXE process. In consequence, its Coulomb interaction $U_{v,c}$ with the core hole in the initial state and the interaction $U_{v,v}$ with the valence hole in the final state will both be negligible small. In this case no double hole satellites are present. In a narrow band material on the other hand, the valence hole can not delocalize that fast, hence the Coulomb interactions have to be taken into account. In most cases, the interaction with the core hole in the initial state is stronger than with the second valence hole in the final state, placing the double hole satellites on the high energy side of the main emission. If the satellite to main line shift is small, the satellite overlaps with the main line, distorting the SXE spectrum.

The interaction of an additional hole present in a narrow valence band with the remaining

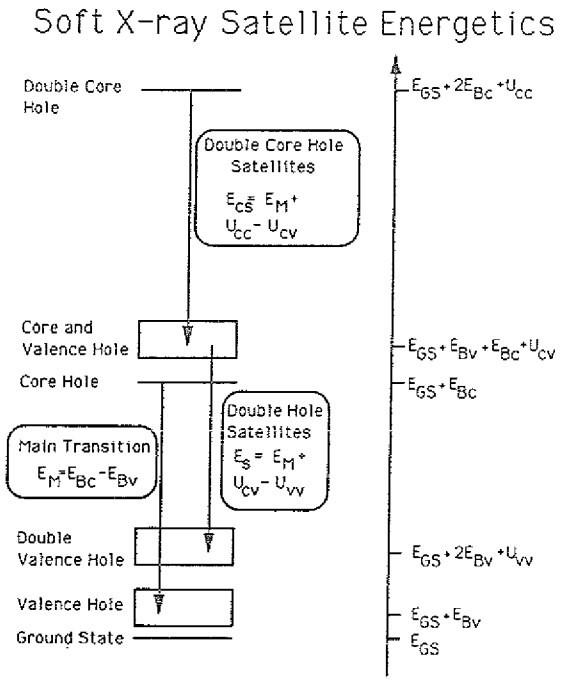

Figure 5: Initial state satellite energetics. The E_i terms denote the energy of the ground state (GS), the binding energy of core (Bc) or valence (Bv) electrons. The U_{ii} terms denote the hole–hole interaction that shifts the total energy of the states involved. The c and v subscripts refer to core and valence levels, respectively. (From [10].)

electrons can be discussed from a different point of view, too. A narrow band indicates small overlap of the atomic orbitals with the orbitals from neighbouring atoms. Thus the interaction between electrons belonging to different atoms is smaller than in a broad band material, where the delocalized electrons can not be viewed as belonging to a specific atom. The situation is somewhat more "atomic-like".

As in atomic systems, *correlation* between the electrons becomes more important. The valence electrons will be influenced by the presence of the valence hole. In this case it is no longer fully appropriate to describe the multi-electron system by independent one-electron wavefunctions, as assumed in the beginning to derive the LPDOS picture of SXE. Thus the spectra seem to be "distorted", when interpreted in terms of the LPDOS.

These distortions and initial state satellites in general can be removed in SXE spectroscopy by selective excitation. Using synchroton radiation as exciting agent [15], one can tune the photon energy just above the threshold for the generation of the initial state core hole. As there is no excess energy available for additional excitations, no initial state satellites appear [16].

In SXA, no initial state satellites exist as the initial state is always the ground state of the system. Nevertheless, electron correlation can be important for narrow band materials in SXA, too, hence making a single-electron description of the transition inappropriate.

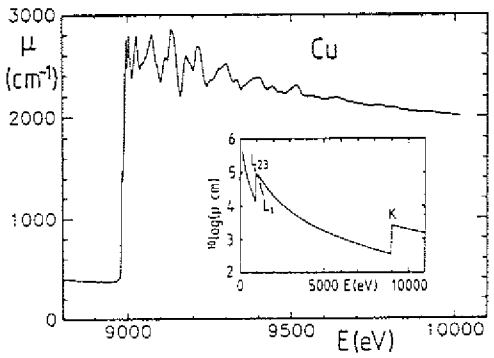

Figure 6: EXAFS oscillations at the Cu K edge. The absorption coefficient $\mu(E)$ is shown as a function of photon energie E. The inset shows a calculation for an extended energy range including the L-edges. (From [20].)

Free electron response. Above we discussed the effect of strong correlation between the valence electrons. In the opposite limit, dynamical effects may become important, too. In many simple metals, where the valence electrons can be regarded as a free electron gas, SXE spectra show a prominent enhancement or damping at the Fermi energy. A similar singularity is then visible at the Fermi energy in the corresponding SXA spectra. The first attempts to understand these singularities made by Mahan [17] were later complemented by Nozières and de Dominicis [18] and resulted in the so-called *MND theory*. According to the MND theory, the observed singularities are due to the response of the (noninteracting) valence electrons to the localized time-dependent pertubation caused by the switching-on (SXA) or switching-off (SXE) of the core hole.

Recently [19] another effect has been claimed to be of at least equal importance for the structures observed at the Fermi energy in XANES spectra. The basic physical idea is that the exciting photon polarizes the core electrons. This polarisation of the ionic core gives rise to dipolar fields which couple to the valence electrons. The effect is enhanced in a resonant way when the energy of the incoming photon equals a core electron binding energy, thus generating the observed features in the vicinity of the Fermi energy.

2.3 Geometric structure

2.3.1 Interpretation of EXAFS in terms of the local geometric structure

Extended x-ray absorption fine structure (EXAFS) refers to the oscillatory variation of the x-ray absorption coefficient μ as a function of photon energy beyond an absorption edge. For isolated atoms, μ decreases monotonically as a function of energy beyond the absorption edge. However, for atoms in molecules or condensed matter, the typical fine structure as shown in Fig. (6) is observed. Approximately the first 40 eV after the absorption edge in the spectrum are thought to be dominated by the DOS effects as described in the XANES section and thus are excluded

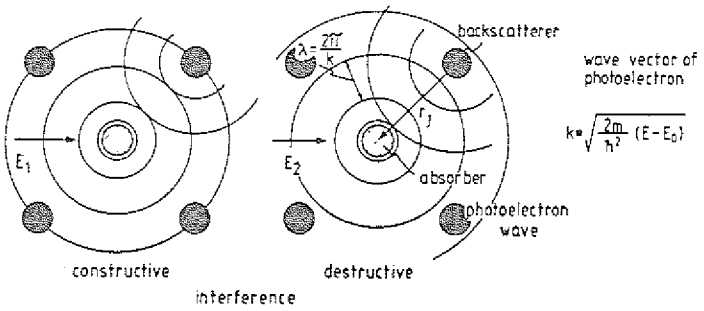

Figure 7: Model to illustrate the origin of the EXAFS oscillations. (From [20].)

from the EXAFS analysis. The basic physical mechanism responsible for the EXAFS oscillations is illustrated in Fig. (7).

The ejected photoelectron can be described as a wave with a certain wave vector k, depending on the energy of the photoelectron. If neighbouring atoms are present, there will be scattering contributions to the outgoing electron wave due to this neighbours. Because of the localized nature of the core orbital involved in the photoemission process, the interference of the backscattered wave with the primary wave at the site of the absorbing atom determines the EXAFS spectrum. A constructive interference will result in a higher probability to excite the electron compared to the case of destructive interference. This is reflected in the detected variations of the absorption coefficient. Thus EXAFS can be described as an interference effect in the photoemission final state caused by single scattering contributions to the photoelectron wave [20, 21, 22, 23].

Fermi's Golden Rule can be applied in the dipole approximation. For a free atom this leads to

$$\mu_0(E) \propto | < f_e|\epsilon\hat{r}|i > |^2 \quad . \tag{8}$$

$|i>$ is the initial state with the electron still in the core orbital while $< f_e|$ denotes the final state where the photoelectron has been ejected without scattering. $\hat{r}$ is the dipole operator and the polarization vector ϵ accounts for a polarisation of the exciting radiation. If neighbouring atoms are present, the final state $< f_e + f_{sc}|$ contains the scattering contribution $< f_{sc}|$. Consequently, the absorption is described by

$$\mu(E) \propto | < f_e + f_{sc}|\epsilon\hat{r}|i > |^2 \quad . \tag{9}$$

The oscillatory part χ of the EXAFS as a function of electron wave vector or energy with respect to the smooth background $\mu_0(k)$ is defined as

$$\chi := \frac{\mu - \mu_0}{\mu_0} \quad . \tag{10}$$

If (a) the wavefunction can be factored into one-electron contributions, (b) the photoelectron can be approximated by a plane wave, (c) the backscattering contribution is small and (d) multiple

scattering can be neglected, then for an initial electron state of s symmetry eqn. (9) can be expressed as [21, 23]

$$\chi(k) = (-1)^l \sum_{i=1}^{n} A_i(k) \sin[2kR_i + \phi_i^l(k)] \quad . \tag{11}$$

The sum is carried out over all contributing shells of backscattering atoms of the same type with a distance R_i to the central absorber atom. l denotes the angular momentum quantum number for the final state, k is the wave vector of the electron as given by

$$k = \sqrt{\frac{2m}{\hbar}(E - E_0)} \quad , \tag{12}$$

where E denotes the energy of the photon absorbed. E_0 is the electron binding energy and m is the electron mass.

Eqn. (11) factores into an amplitude contribution A_i and a phase factor $\sin[2kR_i + \phi_i^l(k)]$. The latter contains length information due to the interference term $2kR_i$, which reflects the idea that the wave described by k travels from the absorber to the scatterer and back again before interfering with the primary wave at the central atom[6]. A second contribution to the phase factor is the phase shift $\phi_i^l(k)$ experienced by the electron because it travels through the electrostatic potentials of the absorbing and backscattering atoms and is backscattered once [24, 23].

The factor $A_i(k)$ describes the contribution of the i^{th} shell to the EXAFS amplitude.

$$A_i(k) = \frac{N_i}{kr_i^2} F_i(k) e^{-2\sigma_i^2 k^2} e^{-2r_i/\lambda_i(k)} \quad . \tag{13}$$

N_i is the effective number[7] of atoms in the i^{th} shell and $F_i(k)$ is the backscattering amplitude corresponding to this type of atom. The next term is a Debye- Waller type factor accounting for thermal vibration of the atoms in a harmonic approximation. Electrons that have suffered inelastic losses will not have the proper wave vector to contribute to the interference process. To account for this effect and the finite core hole lifetime the last damping factor is introduced, crudely modelling these effects by a mean free path $\lambda_i(k)$.

The analytical description of EXAFS at L_3 or L_2 edges is more complicated. This reflects the fact that electron states of s *and* d symmetry can be reached from an initial state of p symmetry. However, the radial matrix element $M_{p,d}$ for a p to d transition is about five times the radial matrix element $M_{p,s}$ for a p to s transition and this ratio is independent of the wave vector for elements with an atomic nuber higher than 20. As a consequence, transitions to the d state are favoured by a factor of about 50 [24]. Thus eqn. (11) can be used with $l = 2$ to describe $L_{2,3}$ EXAFS as well. Note that the phase shifts $\phi_i(k)^l$ are different for waves characterized by different angular momentum quantum numbers l.

[6] This classical picture can not be taken literally. The wave does not travel this way *first* and is *then* interfering. The scattering contributions are present in the outgoing wave all the time.

[7] If one can average over the polarization of the absorbed radiation, this number equals the real coordination number. Using linear polarized radiation, this is possible if the environment around the absorber atom is cubic or isotropic.

There are two basic approaches to analyze EXAFS data, Fourier transformation and curve fitting. Both require the phase shift $\phi_i^l(k)$ as input, which must consequently be known from calculations [24] or additional experiments [20]. From the peaks in the Fourier transformation due to the total phase shift $2kR_i+\phi_i^l(k)$ the interatomic distances R_i can be obtained by correcting for the phase shift $\phi_i^l(k)$. The magnitude of the peaks is proportional to the effective coordination of the central atom in the various shells. The same parameters are obtained in the curve fitting technique by fitting the EXAFS formula (11) to the data. Often a combination of these techniques is used. In the first step the contributions of the different shells are separated by Fourier filtering. In the next step each component is analyzed by curve fitting.

A lot of variants and refinements for various situations have been developped in EXAFS data analysis. The most succsessful concepts are reviewed in the book of B.K. Teo [22].

3 Experimental Details

3.1 Setup for SXA and SXE spectroscopy

SXA spectra were measured using synchrotron radiation at the BESSY synchrotron facility, Berlin. The general setup at the beamlines is shown schematically in Fig. 8. XANES spectra were recorded for the Co L_3-edges of various samples using the 1221 lines/mm-grating of the SX700-2 monochromator [25]. Depending on the exit slit and mirror baffle settings, the energy resolution at 780 eV photon energy is 0.7–1.2 eV. The photon flux was determined by a high transmission gold mesh. Fluorescence radiation was detected 90° from the incident beam direction by a Ge solid-state detector coupled to a multi-channel analyser resulting in an energy resolution of 100 eV at a photon energy of 780 eV. Thus we were able to select the Co $L_{2,3}$-radiation in a partial yield mode. Additionally to this partial fluorescence yield, the total electron yield was recorded by a channeltron, 45° from the beam direction.

EXAFS spectra of the Co L edges were measured using the same setup as described above at the HE-PGM-2 beamline [26] at BESSY with a resolution of about 2 eV.

SXE spectra were recorded in a spherical grating grazing incidence spectrometer (Fig. 9) [27], using 3 keV electrons and the second harmonic of the X1B undulator beamline at NSLS [28] for excitation and in a crystal spectrometer [29, 30], using Cu K and L fluorescent excitation. The best resolution, around 0.6 eV, was achieved in the 2^{nd} order of diffraction with a 10 micron input slit, and a 5m grating with a groove density of 1200 g/mm. The spectra were calibrated using the spectrum of cobalt metal.

3.2 Sample preparation by IBS

$CoSi_2$ layers buried in Si(100) and Si(111) were provided by R. Jebasinski and S. Mantl (Institut für Schicht- und Ionentechnik, Forschungszentrum Jülich). They were produced by ion beam synthesis (IBS) [7, 4].

This preparation technique is shown schematically in Fig. 10. The samples were prepared by 100 keV Co ion implantation into Si(100) or Si(111) wafers at a temperature of 375°C. The implantation dose was $1.4\ 10^{17}$ atoms/cm^2.

The resulting Co concentration profile in the wafer as measured by Rutherford backscattering spectroscopy (RBS) is scetched in Fig. 10a. Silicide precipitates in the as-implanted specimen are observed in cross-sectional transmission electron microscopy (XTEM).

These samples have been annealed at 600 °C for one hour followed by 1000 °C for 30 minutes. The annealed specimens (Fig. 10b) consist of a single crystalline, stoichometric $CoSi_2$ layer of about 500 Å thickness with sharp interfaces buried under a 270 Å Si cap layer, as verified by RBS [7, 4]. A XTEM picture of a similar sample is shown in Fig. 11.

In addition to the buried layers a $CoSi_2$ single crystal and Co (polished and sputtered) were investigated.

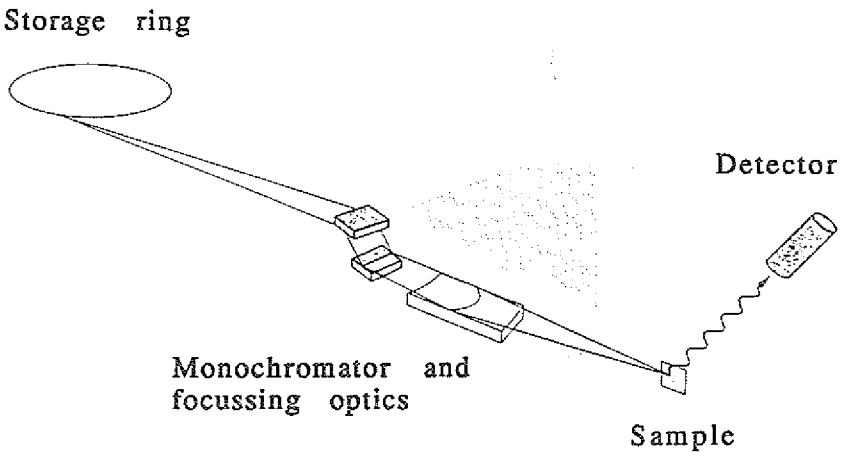

Figure 8: Schematic picture of the experimental setup at a synchroton beamline. The synchroton radiation is generated in a magnetic structure of the storage ring, can be monochromatized in the beamline and is focussed on the sample.

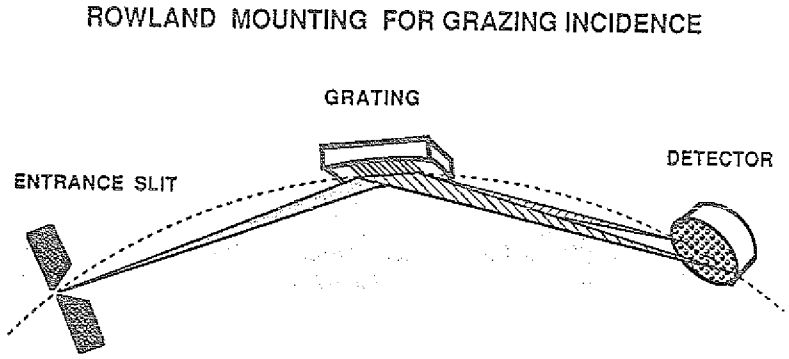

Figure 9: Principle of operation of the spherical grating grazing incidence spectrometer. The dispersive element is a spherical reflection grating used in grazing incidence. As it is mounted in a Rowland setup, it focusses the radiation on a position sensitive detector. Entrance slit, grating and detector are positioned on a Rowland circle (dashed line).

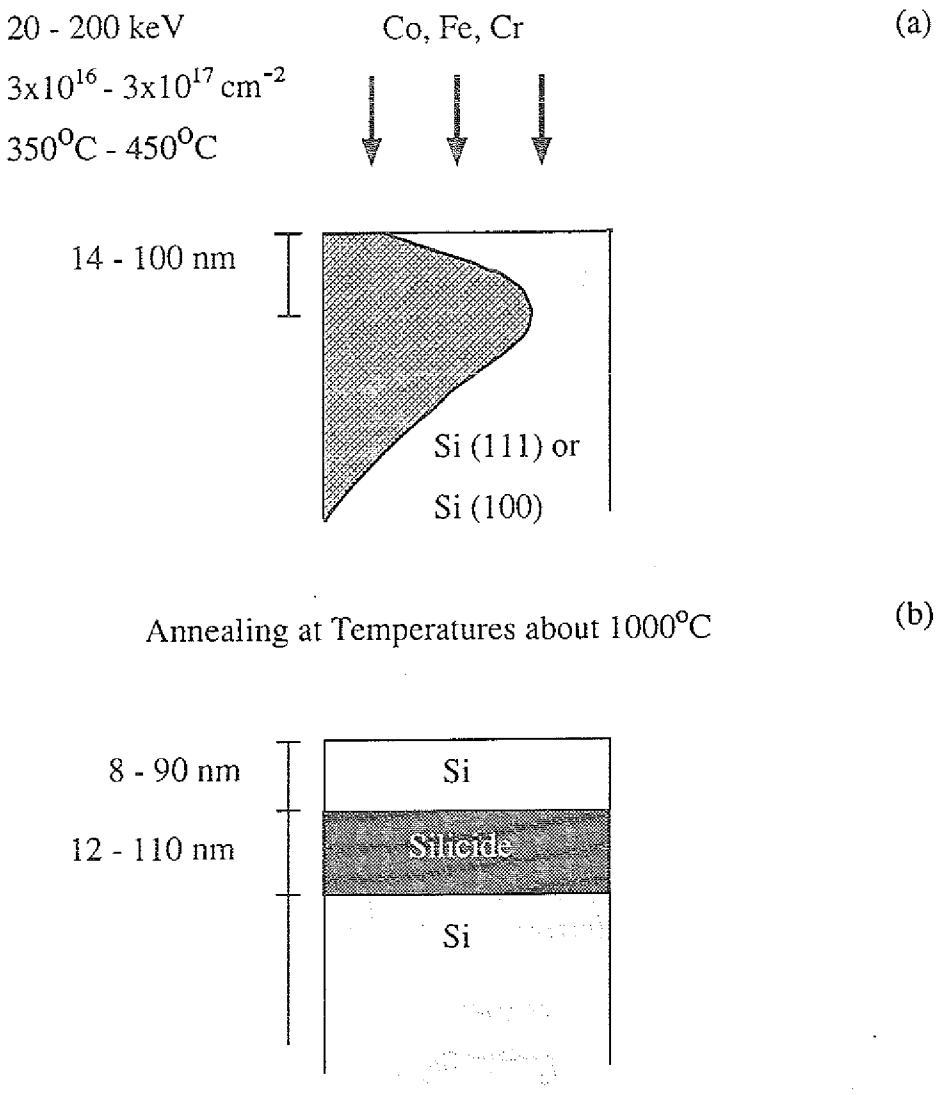

Figure 10: Preparation of a buried silicide layers in a Si wafer by means of IBS. After TM implantation (a), silicide precipitates can be observed in the as-implanted samples, resulting in the scetched Co concentration profile (a). Upon annealing, a crystalline $CoSi_2$ layer with sharp interfaces is formed (b).

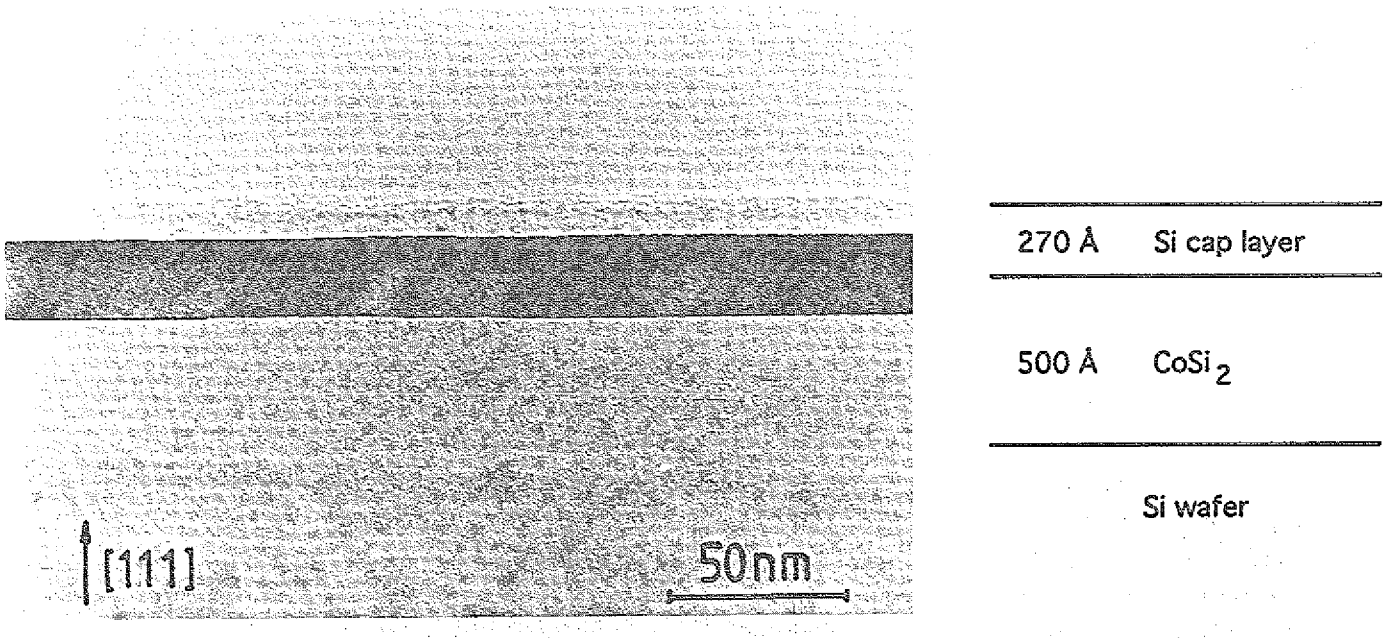

Figure 11: Bright-field XTEM micrograph of a $CoSi_2$ layer buried in Si(111) by IBS. The thickness of the Si cap layer and the silicide layer for the samples investigated is indicated in the scheme at the right side.

4 Method Development

4.1 $L_{2,3}$ EXAFS for 3d transition metal silicides

4.1.1 Introduction

In this section we want to present the advantages and limitations in the analysis of EXAFS measurements at the transition metal $L_{2,3}$ edges of 3d transition metal (TM) silicides which are buried in Si wafers.

As pointed out in a previous section, EXAFS spectroscopy is a unique tool for the study of the local geometric structure. For 3d TMs, EXAFS investigations of the TM K edges (K-EXAFS) are quite common, while experiments analysing the TM L edges (L-EXAFS) are very rare.

However, for an *in situ* analysis of a layer buried in a crystalline Si wafer, L-EXAFS is favourable, as it can be combined with FY detection of x-ray absorption. The FY detection mode has to be used for this kind of samples, as
(a) the sample is too thick to measure the EXAFS in the transmission mode and
(b) the x-ray absorption can not be monitored by EY due to the short electron escape depth.

The main problem for an FY K-EXAFS measurement on these systems are the Bragg diffraction beams generated in the Si wafer. Due to the crystallinity of the wafer and the high photon energies required for K-EXAFS ($E_{Co\,K} \simeq 7709\ eV$) a lot of extremely intense Bragg diffraction beams are generated. When scanning the photon energy some of them hit the fluorescence detector and distort the spectra severely, making an EXAFS analysis impossible [31]. In contrast, this is no problem in L-EXAFS, as no Bragg diffraction peaks are present due to the lower photon energies ($E_{Co\,L_3} \simeq 793\ eV$)

Despite of these problems, K-EXAFS of buried 3d TM silicides has recently been reported, using a setup where the Bragg diffraction beams were selectively blocked in front of the detector [32]. This gives us the opportunity to compare L-EXAFS and K-EXAFS for these systems.

An additional advantage of L-EXAFS for 3d TM compounds is the fact that the XANES region gives insight into the local d DOS at the TM atom. The d states are of utmost importance for the electronic properties and the chemical bonding in these compounds. Using SXA spectroscopy at the TM L edges it is thus possible to determine the electronic and the geometric structure with the same setup.

However, EXAFS spectroscopy at the 3d TM $L_{2,3}$ edges is difficult because of two reasons. First, the L edges of the 3d TMs are located in the soft x-ray region. This poses certain experimental difficulties. The experiments have to be carried out in an UHV system. Additionally, gratings and mirrors have to be used to monochromatize the radiation in contrast to crystal monochromators. Nevertheless, high performance beamlines have been developed in the last years [25, 28]. Coupled to synchroton radiation sources they produce the necessary high flux of monochromatized photons in the soft x-ray range.
The second difficulty in L-EXAFS experiments of 3d TMs is posed by the data analysis, which is not as straightforward as in K-EXAFS. The main problems for such a L-EXAFS analysis for 3d TMs are the superposition of the EXAFS structures produced by the L_3 and L_2 edges and the

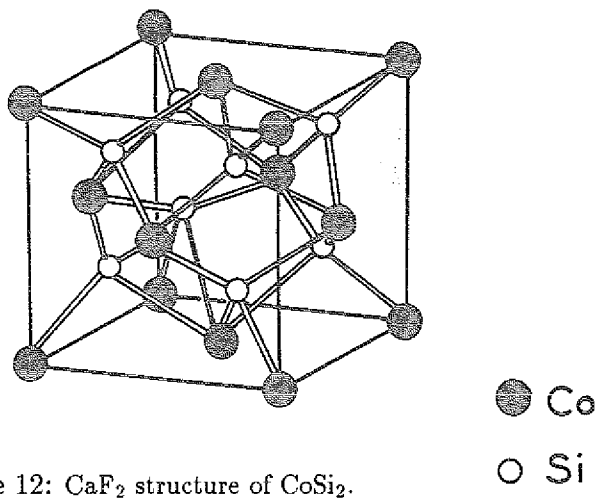

Figure 12: CaF_2 structure of $CoSi_2$.

additional superposition of the L_1 absorption [33].

It is the aim of this section to investigate how L-EXAFS can be analysed for these systems.

We have chosen a $CoSi_2$ layer buried in a Si(100) wafer [7] as described in the sample preparation section for this investigation. Pure $CoSi_2$ crystallizes in the cubic CaF_2 structure with a unit cell edge length of 5.365 Å [34]. From the viewpoint of a Co central atom, this results in 8 first shell Si neighbours at a distance of 2.323 Å and 12 second shell Co neighbours at a distance of 3.794 Å (See Fig. 12).

4.1.2 $L_{2,3}$ EXAFS data analysis

Figure 13 shows an SXA spectrum of a $CoSi_2$ layer buried in a (100)Si wafer recorded by FY detection. Above the L_3 and L_2 absorption edges strong EXAFS wiggles are clearly visible up to the end of the spectrum. An additional feature is produced by the onset of the L_1 absorption at about 925 eV.

This poses two questions with respect to an EXAFS analysis:

1. How does the superposition of the L_3 and the L_2 EXAFS influence the analysis?
2. How can the additional superposition of the L_1 absorption be handled in the analysis?

The EXAFS wiggles due to the L_2 absorption are characterized by the same periods as the structures produced by the L_3 absorption, as they are due to the same geometric structure. However, they are shifted by about 15 eV to higher energies because of the $L_{2,3}$ spin-orbit splitting in Co. The relative intensities between the wiggles generated by ejecting $2p_{\frac{3}{2}}$ electrons (L_3 absorption) and $2p_{\frac{1}{2}}$ electrons (L_2 absorption) should be 2:1, reflecting the different degeneracy of the excited states. As the spin-orbit splitting of 15 eV is small compared to the typical EXAFS oscillations period of about 60 eV in $CoSi_2$, the effect of this superposition is small with respect to the determination of interatomic distances [35]. The influence of the spin-orbit splitting is of course even smaller for the earlier 3d TMs ($\Delta E_{Sc} = 4.9$ eV) but might become a more serious problem for the late TMs ($\Delta E_{Zn} = 23.1$ eV) (see Table 2).

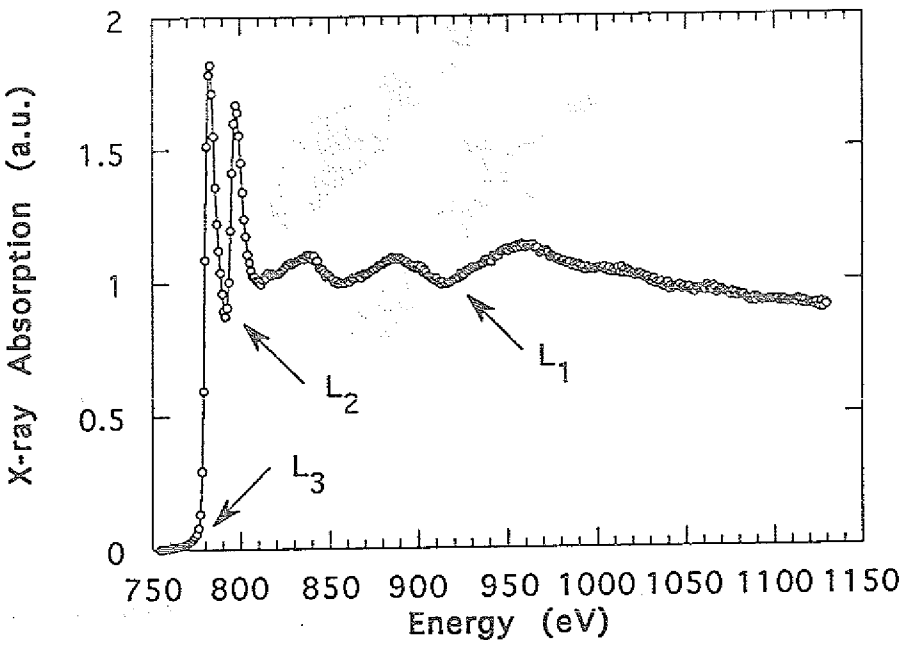

Figure 13: X-ray absorption as a function of photon energy of IBS $CoSi_2$ monitored by FY detection. The three Co absorption edges are indicated by arrows. In the energy range above 925 eV, additional background due to the Co L_1 absorption is superposed to the Co $L_{2,3}$ EXAFS oscillations.

The effect of the $L_{2,3}$ superposition on the amplitude of the wiggles can not be neglected. Due to this superposition the amplitude of the EXAFS oscillations is reduced relative to the edge jump[8], which is defined as the total rise of the absorption coefficient at the absorption edge. (The XANES features close to the absorption threshold are not included in the definition of the edge jump.)

The magnitude of the reduction depends on the ratio of the spin-orbit splitting to the period of the oscillations. The amplitude is furthermore reduced by saturation effects due to the FY detection [9, 36] as described in section 4.2.

In an EXAFS analysis, the number of atoms in the various shells around the central atom is determined from the amplitude of the wiggles relative to the edge jump.

Though it is in principle possible to account for the two amplitude reducing mechanisms discussed above, these effects make an absolute determination of coordination numbers difficult. We will focus our attention to the determination of the interatomic distances in the following.

The problems posed by the superposition of the L_1 absorption to the $L_{2,3}$ EXAFS structures are much more severe. The photoabsorption cross-section for the Co $2s$ electrons just above the $2s$ threshold is about 15% of the cross-section for the Co $2p$ electrons [37, 38]. Thus the near edge structure produced by the $2s$ electrons is of about the same magnitude as the $L_{2,3}$ EXAFS wiggles due to the $2p$ electrons, whose amplitudes are about 5 % of the L_3 edge jump in $CoSi_2$. The effect

[8]To illustrate this reduction one can immagine the extreme case where the two superposed spectra characterized by the same oscillation period are shifted relative to each other by half the period.

of this superposition is clearly visible in Fig. (13). The strong absorption in the energy range between 920 and 960 eV indicates the presence of the L_1 absorption, whose onset is expected at 925.1 eV [39]. In addition, the slope of the background changes in the energy range above 960 eV according to presence of the new absorption channel.

Though the presence of the L_1 edge in the SXA spectrum is obvious, it is impossible to immediately deduce its shape from the spectrum because of its interference with the $L_{2,3}$ EXAFS. As the shape of the Co L_1 absorption is not known, we try to remove this additional background empirically by a special splining procedure. In the following we will discuss this technique and the results obtained.

A set of cubic splines has been used to account for the smooth background μ_0 produced by the atomic absorption in EXAFS measurements [40]. For this purpose, the EXAFS spectrum is divided into equidistant intervals. On each interval, a cubic spline interpolation is performed under the condition, that the splines have to match at the interval boundaries. We will call the resulting function a "polyspline". Choosing the length of the intervals appropriate, this cubic polyspline is too 'stiff' to follow the individual EXAFS oscillations but will follow the mean trend of the data. By means of this procedure the atomic background μ_0 is modelled by the polyspline and can be used to determine $\chi(k)$ as defined in eqn. (10).

A similar polysplining technique can be used to account for the additional background due to the Co L_1 edge. If the order of the spline polynomial is increased, it will become less 'stiff' and thus be able to follow the spectral features more closely. In order to use this procedure to account for the additional L_1background, the spline intervals have to be chosen properly. The aim is to 'soften' the polyspline only in the region where the L_1 absorption is expected. (See Fig. 14 as an example.) This techique has recently been used for surface EXAFS measurements at the Co $L_{2,3}$ edges in $CoSi_2$ [35].

As the shape of the spline can be influenced to a large extent, it is important to have criteria judging the quality of the spline approximation. Apart from direct information about the shape of the L_1 absorption, which is quite limited, the resulting Fourier transform can be used to judge the quality of the spline used. Strong peaks in the tansform at distances around 1 Å reflect no physical property of the $CoSi_2$ system. Their appearence is thus an indication of poor polysplining. A second criterion is the shape of the first shell peak in the Fourier transform. As this first shell is well separated from the second shell in $CoSi_2$, the corresponding peak in the Fourier transform should be symmetric with respect to the peak position.

We will in the following present an EXAFS analysis of the spectrum shown in Fig. 13. Using two different polysplines, we will discuss the advantages and limitations of the L-EXAFS technique and compare it to the K-EXAFS results of a similar system[32, 41].

4.1.3 Results and Discussion

The following steps of data processing were made for each of the polysplines used. Each step is documented in a figure. (See table 1).

Overview of the EXAFS figures		
Polyspline No.	1	2
Initial data and polyspline	Fig. 14	Fig. 19
$\chi(E)$	Fig. 15	Fig. 20
Fit to $[k\,\chi(k)]$	Fig. 16	Fig. 21
Fourier transformation of $[k\,\chi(k)]$ and fit	Fig. 17, Fig. 18	Fig. 22

Table 1: Overview of the EXAFS figures corresponding to the various steps of data analysis.

Polysplining. In both cases, the polyspline is produced using three spline intervals. The first interval always starts at 824 eV, *i.e.* about 30 eV above the L_2 threshold energy, and extends to about 920 eV. In this region the order of the spline is 2, *i.e.* a linear polynomial is used. The next interval extends to about 970 eV. The exact length ot this interval is different for the two different polysplines. This parameter was used to model different shapes of the L_1 background absorption. A spline of order 4 has been found most suitable to account for the L_1 absorption present in this energy range. The last interval extends up to the end of the spectrum at 1130 eV. Best results were achieved using a cubic spline to account for the background in this region.

Determination of $\chi(E)$. Assuming that the polyspline represents the atomic background absorption μ_0, $\chi(E)$ was determined according to eqn. (10).

Curve fitting to $[k\,\chi(k)]$. χ was transfered to the wave vector scale using $E_0 = 776\ eV$ as zero energy for the determination of the k scale origin[9]. $\chi(k)$ was weighted by k to account for the damping of the structures at higher k. Using the program EXCURV90, the Co–Si and Co–Co phaseshifts were calculated for the L edges and a curve fit of the basic EXAFS formula (11) to the data was performed. EXCURV90 uses curved wave theory [43, 44, 45] to simulate an EXAFS spectrum. The nearest neighbour distances R_i, the coordination numbers N_i, and the adjustment of the k scale origin were varied to find the best fit to the experimental data.

Fourier transformation of $[k\,\chi(k)]$ and the fitted curve. The experimental data and the simulated spectrum with the best fit were both Fourier transformed. Note that the x-axis does not exactly measure interatomic distances as the phase shift can not be fully taken into account in the Fourier transformation. The distances are determined by the fitting procedure. The Fourier transforms of theory and experiment are used as a crosscheck upon this determination. For the shell investigated they should peak at the same distance.

In Fig. 14 we present the measured x-ray absorption (open circles) and the polyspline No. 1 (solid line). A broad L_1 edge is modelled in the energy range between 920 eV and 970 eV. The

[9]This energy was estimated by the method of Lee and Beni as described by B.K. Teo [22]. The basic idea is that the imaginary part of a complex Fourier transform of an EXAFS spectrum described by eqn. (11) should peak symmetrically at peaks of the absolute value of the Fourier transform, if the k origin and the phase shifts $\phi_i'(k)$ have been chosen correct.

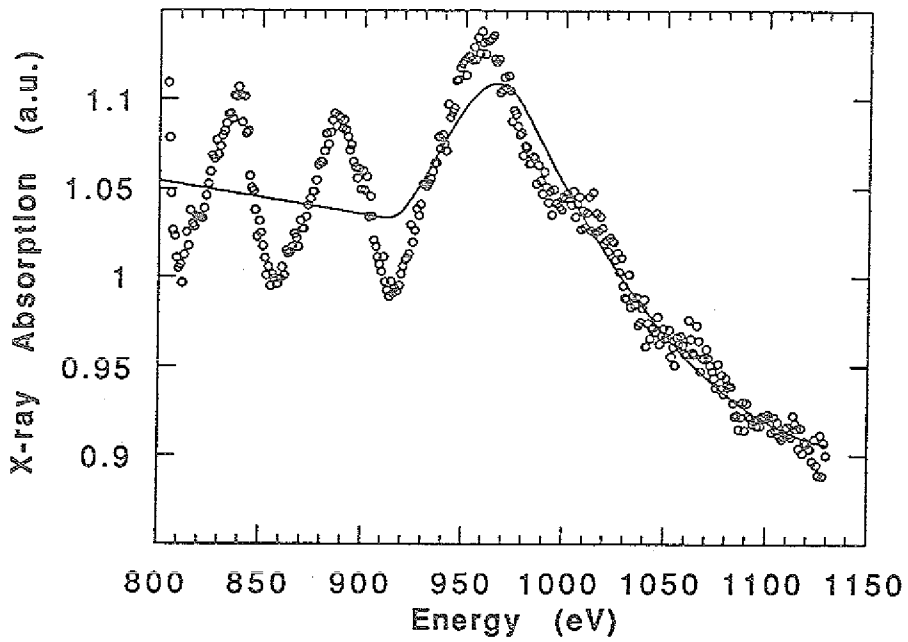

Figure 14: X-ray absorption of IBS $CoSi_2$ as presented in Fig. 13 (circles) and polyspline No. 1 (solid line).

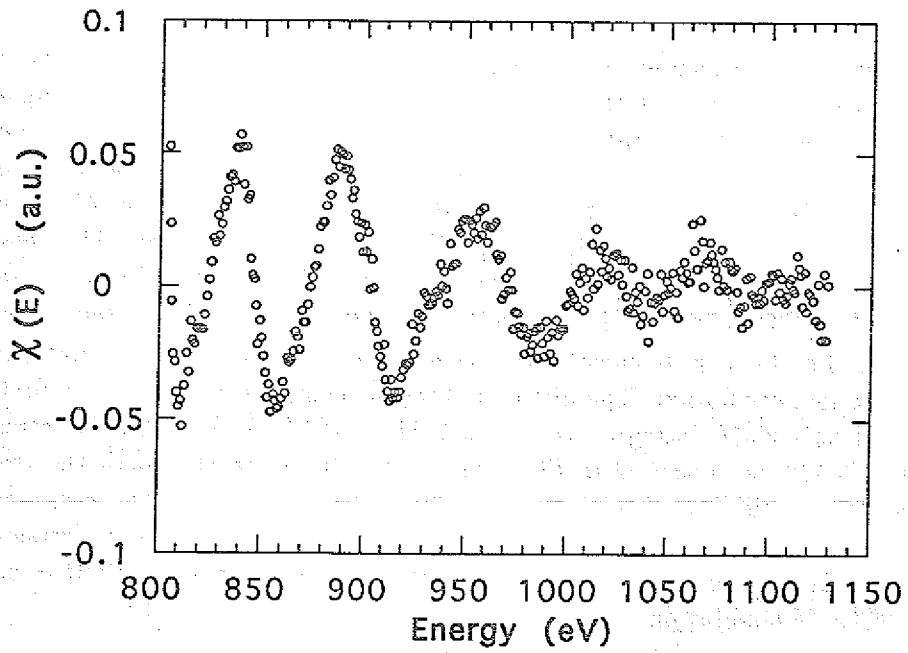

Figure 15: This figure shows the oscillatory part $\chi(E)$ of the EXAFS presented in Fig. 14 as a function of photon energy. It was calculated according to eqn. (10) using polyspline No. 1.

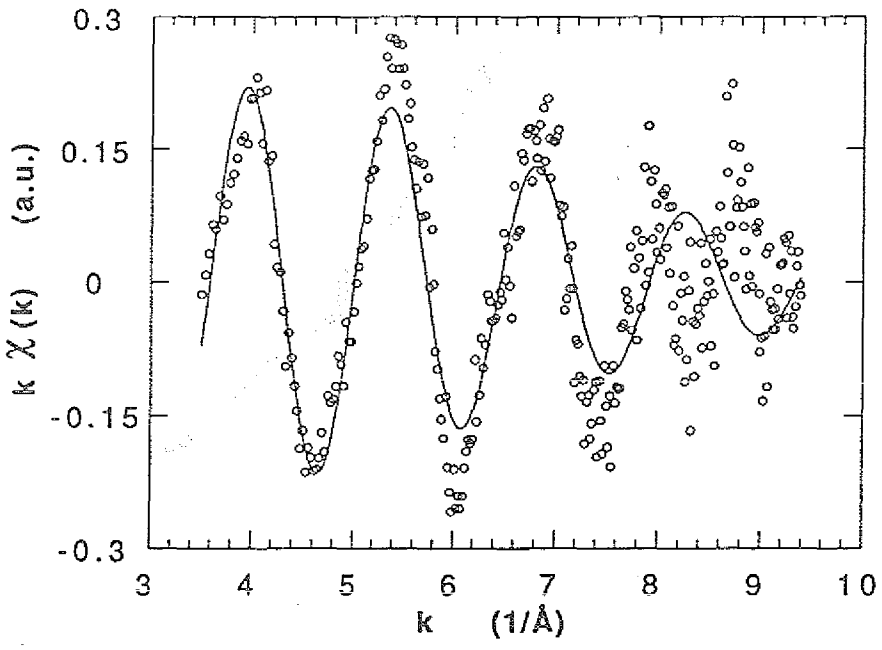

Figure 16: The circles represent the k-weighted $\chi(k)$ as derived from the data in Fig. 15 according to eqn. (12). The solid line represents the single-shell simulation of the EXAFS spectrum with the best fit to the data (see text for details). The simulation parameters are $R_1 = 2.317$Å and $E_0 = 775.46\,eV$.

$\chi(E)$ spectrum derived using this polyspline is presented in Fig. 15. The strong absorption feature present around 940 eV in the initial data is reduced, resulting in a smoothly decreasing amplitude envelope in $\chi(E)$. In Fig. 16, χ is transfered to the k scale and multiplied with k to account for the damping before curve fitting and Fourier transformation. The Fourier transform of $[k\,\chi(k)]$ is shown in Fig. 17 (solid line). The transform is dominated by the peak at 2.2 Å, which can clearly be attributed to the first coordination shell. No distinct second or third shell contribution can unambigiously be attributed to the other peaks present. Thus, we fitted a single shell model to $[k\,\chi(k)]$ in Fig. 16. The solid line in this figure represents the caculated spectrum with the best fit to the data. The fit is quite close to the data points up to $k = 7.2\,\text{Å}^{-1}$, but out of phase with the data in the last oscillation. The distance from the central Co atom to the first shell was determined in the EXCURV90 fitting procedure as 2.317 ± 0.006 Å. The Fourier transformation of the calculated EXAFS is presented in Fig. 17 (broken line) together with the transform of the experimental data (solid line), confirming that the prominent peak in the Fourier transform of the experimental data is due to the first shell contribution. As theory and experiment peak at the same position, this distance can be assigned to the first neighbour distance R = 2.32 Å used to calculate the EXAFS simulation.

This analysis using the polyspline No. 1 demonstrates that the L- EXAFS of buried $CoSi_2$ generated by ion beam synthesis can be succsessfully used to determine the first shell Co–Si distance. The presence of the first shell signal is obvious in the Fourier transformation and can be assigned to a distance of 2.32 Å. The error in this value is certainly higher than indicated

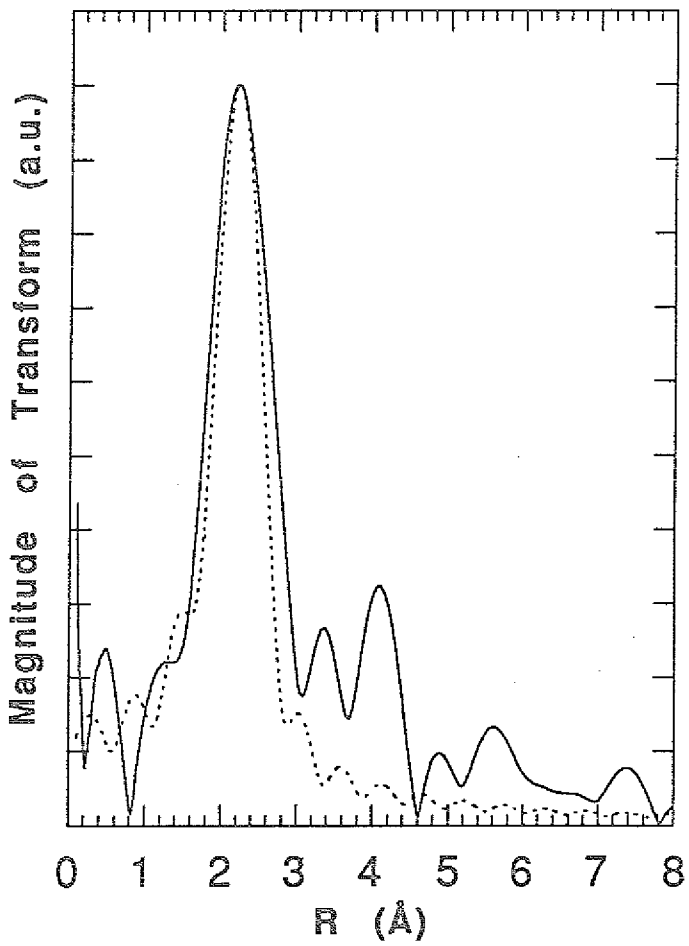

Figure 17: Fourier transform of the experimental data (solid line) and theory (dotted line) presented in Fig. 16.

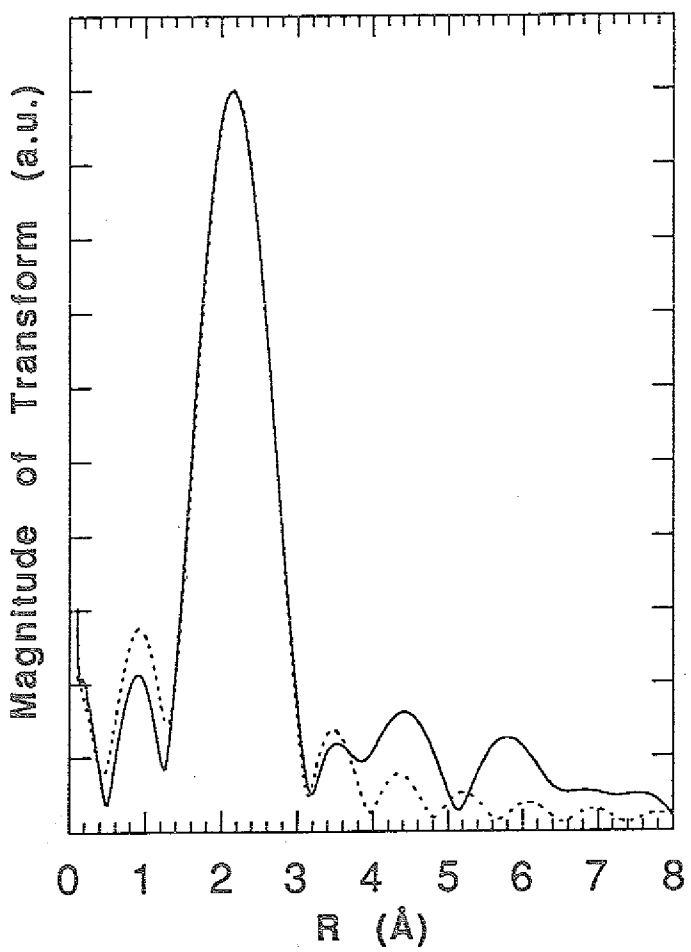

Figure 18: Fourier transform of the experimental data (solid line) and theory (dotted line). In contrast to Fig. 17, the data presented in Fig. 16 was truncated at $k_{max} = 7.2\text{Å}^{-1}$ and Fourier transformed on this restricted wave vector range.

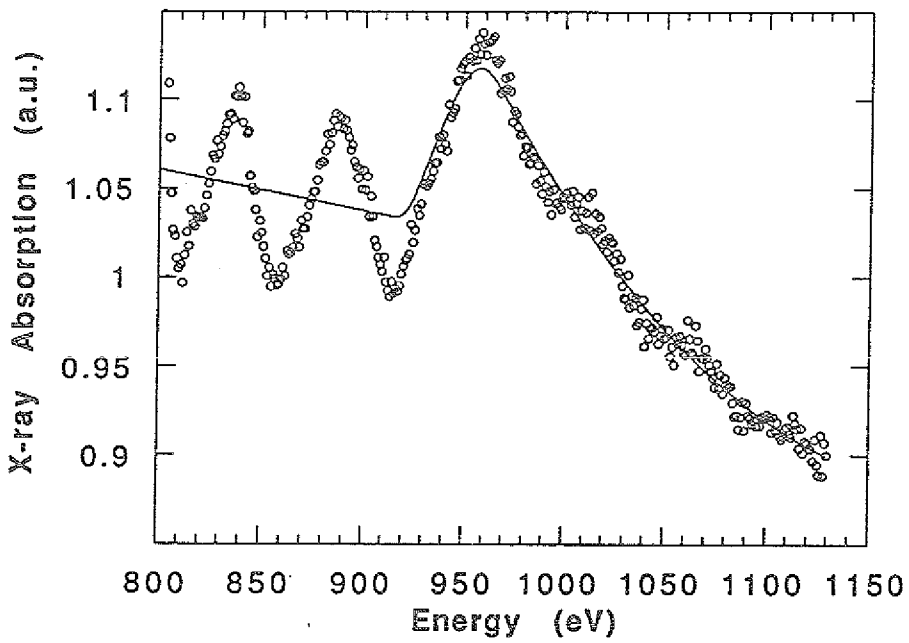

Figure 19: X-ray absorption of IBS $CoSi_2$ as presented in Fig. 13 (circles) and polyspline No. 2 (solid line).

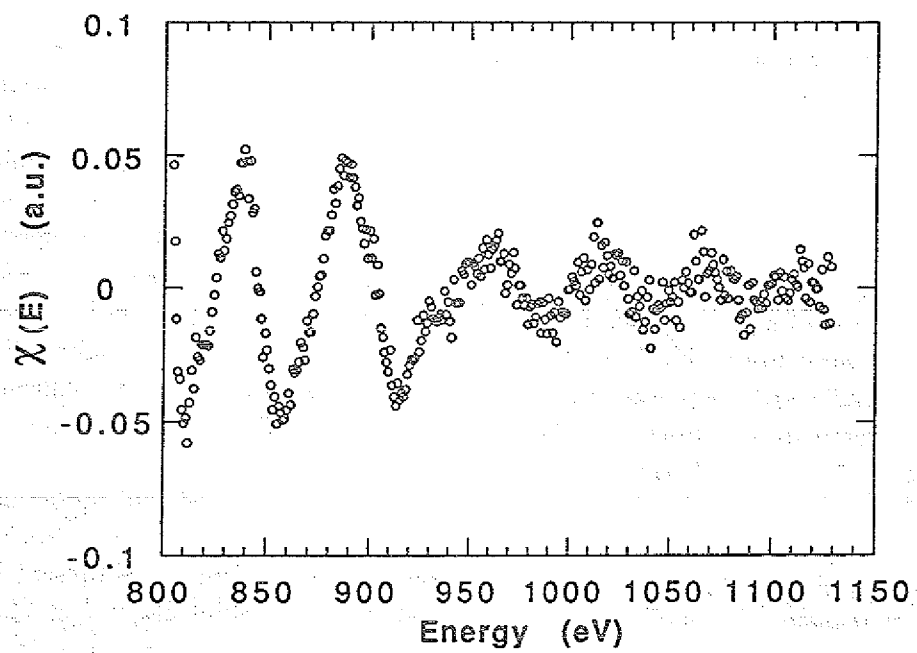

Figure 20: In this figure we present the oscillatory part $\chi(E)$ of the EXAFS shown in Fig. 19 as a function of photon energy. It was calculated according to eqn. (10) using polyspline No. 2.

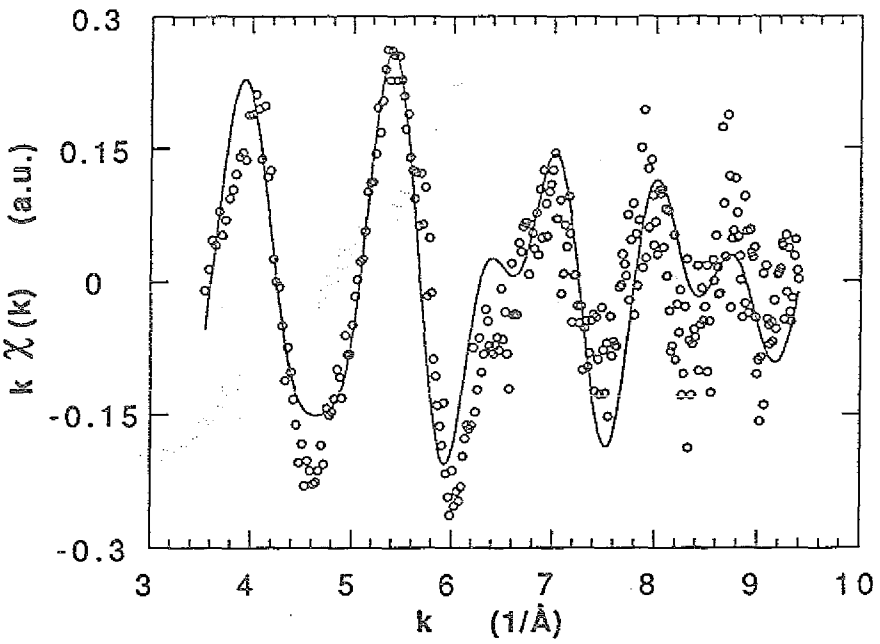

Figure 21: The circles represent the k-weighted $\chi(k)$ as derived from the data in Fig. 20 according to eqn. (12). The solid line represents a two-shell simulation of the EXAFS spectrum using the literature values $R_1 = 2.323$Å and $R_2 = 3.794$Å. ($E_0 = 775.46\,eV$, see text for details.)

by the fitting procedure and is estimated to be $\pm$ 0.05 Å due to uncertainty in the data and the influence of the polysplining procedure. The distance is in perfect agreement with the value 2.323 Å expected for crystalline $CoSi_2$. This agreement is at first sight surprising, as the EXAFS simulation does not fit the data for $k > 7.2\text{Å}^{-1}$ well. However, the agreement indicates that the information about this first shell distance was mainly extracted from the low wave vector part of the spectrum ($k < 7.2\text{Å}^{-1}$). As the L_1 edge modelling starts in the polyspline at about $k = 6\,\text{Å}^{-1}$, the influence of the polyspline is small in this range. Thus the first neighbour distance can be determined with high accuracy as it does not strongly depend upon the shape of the spline modelling the L_1 absorption. Evidence for this hypothesis is presented in Figure 18. Here, the experimental EXAFS spectrum was cut of at $k = 7.2\text{Å}^{-1}$ before Fourier transforming on this restricted wave vector range. Both first shell peaks agree perfectly in the shape and the position corresponding to the best fit distance of 2.317Å.

Now, an EXAFS analysis on the same input data using a different polyspline is presented. Choosing the upper boundary of the 'soft-splining' interval lower as in polyspline No. 1, polyspline No. 2 models a steeper L_1 edge (see Fig. 14). The resulting $\chi(E)$ function is presented in Fig. 20 and the Fourier transformation of the data is represented by the solid line in Fig. 22.

In the Fourier transform, two prominent peaks can be seen. The peak associated with the first Co–Si shell is at the same position as in the analysis which used the polyspline No. 1. This finding again corroborates the hypothesis, that this information is mainly extracted from the first part of the $\chi(k)$ spectrum and thus not strongly affected by the L_1 modelling. The larger FWHM

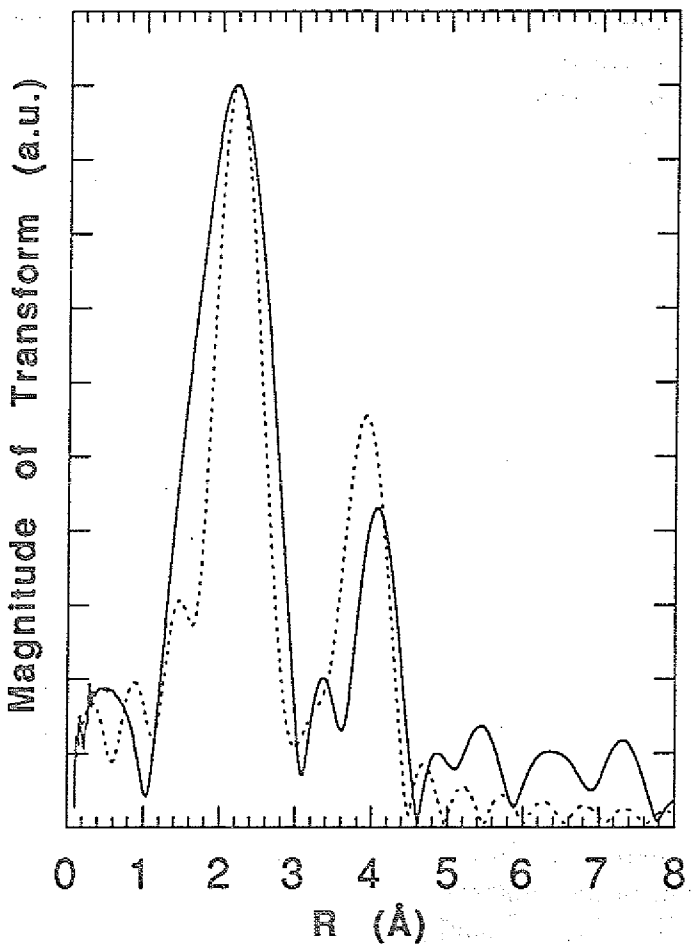

Figure 22: Fourier transform of the experimental data (solid line) and theory (dotted line) presented in Fig. 21.

of the first shell peak derived by using polyspline No. 2 instead of polyspline No. 1 indicates that the information is extracted from a shorter wave vector range. In addition to this peak, a second prominent peak can be seen at about 4 $Å^{-1}$. As this peak in the Fourier transform is considerably higher than the remainig structures, it seems possible that this peak corresponds to Co–Co second shell contributions to the EXAFS. To check this hypothesis, an EXAFS spectrum was simulated including the second shell contributions. This simulation is shown as the solid line in Fig. 21. Here, the theory was not fitted to the data, instead the literature values for $CoSi_2$, $R_1 = 2.323$ Å and $R_2 = 3.794$ Å, were used. Though the simulated EXAFS does not fit the data as well in the low k range as the single shell fit presented in the context of the polyspline No. 1, the behavior in the high k regions seems to bee in better qualitative agreement with the experimental data. Note that the antiphase behaviour between theory and experiment present in Fig. 16 in this k range is no longer observed in Fig. 21. The qualitative agreement of the simulated spectrum with the data indicates the presence of second shell information in the experimental data. However, the second shell distance of 3.89 Å as determined by a Fourier transformation including the Co–Co phaseshift is 0.2 Å bigger than the literature value of 3.695 Å. This indicates the strong influence of the polyspline in the wave vector range above 6 $Å^{-1}$ and can be taken as an estimate of the errors due to the polyspline method in this region.

In Fig. 23 we compare the Fourier transforms obtained in the Co L-EXAFS analysis presented above to results published by Tan *et al.* for a similar system [32, 41]. Spectra (a) and (b) are the Fourier transforms obtained in the L-EXAFS analysis using the polysplines No. 2 and No. 1, respectively. They have already been presented in Figs. 22 and 17. The x-axis has been shifted to align the first shell peaks with the corresponding peaks in the Fourier transformations in (c) and (d). This shift occurs due to the fact that in our transformations the Co–Si phaseshift has been taken into account in contrast to the spectra (c) and (d) presented by Tan *et al.* [32]. Spectrum (c) is the Fourier transform of an annealed $CoSi_2$ IBS sample obtained by analysing the Co K-EXAFS. The initial implantation dose of $1.0\,10^{17}\ Co/cm^2$ for this sample was slightly lower than for our $1.4\,10^{17}\ Co/cm^2$ sample. Spectrum (d) is the Fourier transform of a bulk $CoSi_2$ reference sample, which has been analysed using K-EXAFS by Tan *et al.*.

Comparing the Fourier transforms produced by L- and K-EXAFS, it is obvious that the same structural information is contained. All spectra show a dominant peak due to the first shell scattering contribution around 2.0 Å. A second shell peak is clearly visible in transforms (a), (c) and (d) at about 3.6 Å, in transform (b) it is present but less pronounced. Tan *et al.* determine the first shell distance in the annealed IBS sample (spectrum (c)) as 2.32 ± 0.02 Å, which is in perfect agreement with the value 2.32 ± 0.05 Å determined in the L-EXAFS analysis (spectra (a) and (b)). The possible error in the determination of the first shell distance is slightly lower in the analysis of Tan *et al.*. This fact is reflected in the lower FWHM of the first shell peaks and is due to the larger wave vector range extending from 2.5 $Å^{-1}$ to 13.5 $Å^{-1}$ covered in the K-EXAFS experiment. The distance of the second shell has not been determined from the K-EXAFS experiment. As shown above, this distance can only be evaluated with a large error as 3.9 ± 0.3 Å in our L-EXAFS experiment due to the strong influence of the polyspline.

Thus, the two methods produce the same results. As both samples can be assumed to be

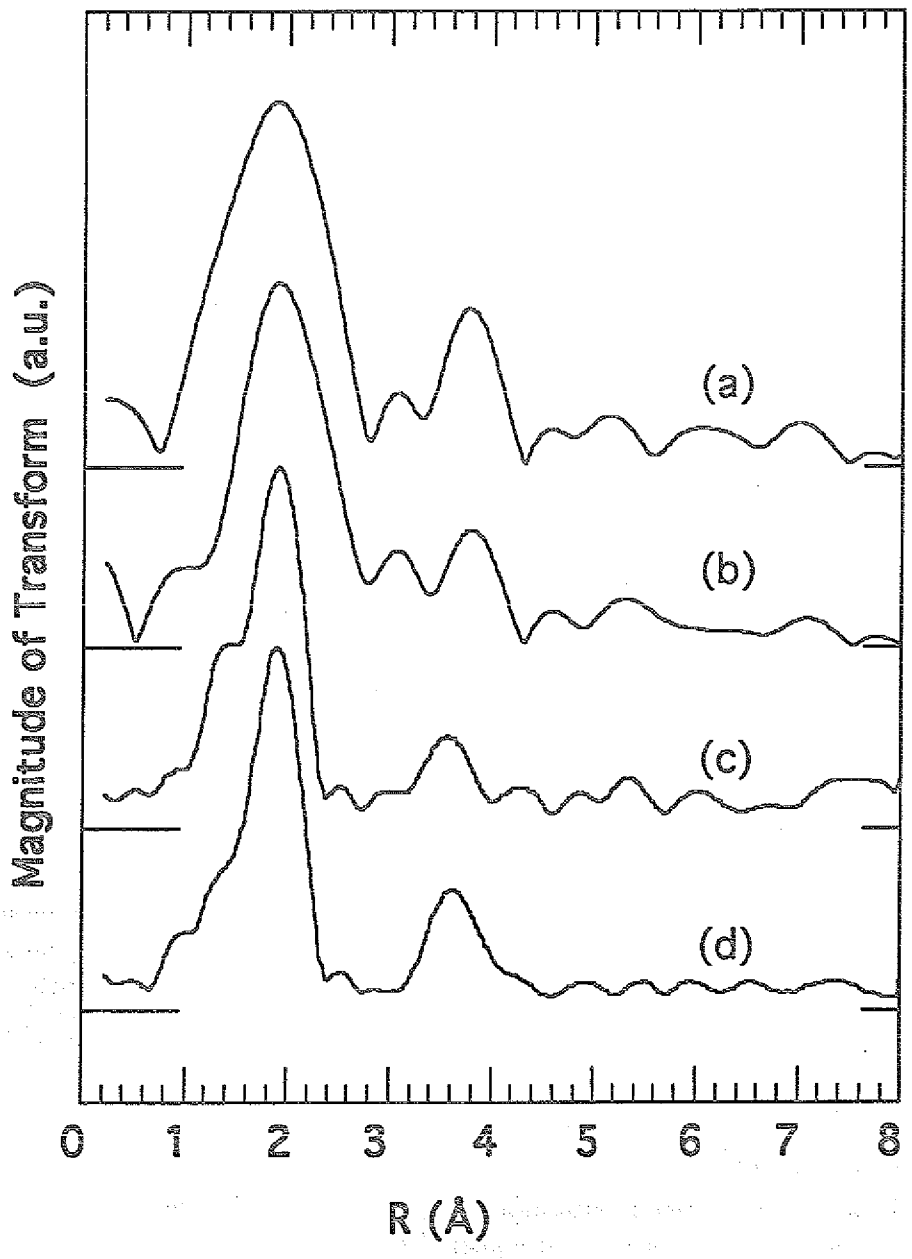

Figure 23: In this figure we compare Fourier transformes obtained in EXAFS analysis of $CoSi_2$ systems. (a) and (b): annealed 1.010^{17} Co/cm^2 IBS $CoSi_2$ sample analysed by Co L-EXAFS. In (a) polyspline No. 2 was used, (b) was obtained using polyspline No. 1. (c): annealed 1.410^{17} Co/cm^2 IBS $CoSi_2$ sample analysed by Co K- EXAFS by Tan *et al.* [32]. (d): Bulk $CoSi_2$ reference sample analysed by Co K-EXAFS by Tan *et al.*[32].

Element	$\Delta E_{L_3-L_2}\,(eV)$	$\Delta E_{L_3-L_1}\,(eV)$
Sc	4.9	99.3
Ti	7.4	107.1
V	7.7	114.6
Cr	9.7	121.6
Mn	11.2	130.4
Fe	13.1	137.8
Co	15.2	147.0
Ni	17.3	155.9
Cu	19.8	164.2
Zn	23.1	174.4

Table 2: Overview of the energy separation between the L_3, L_2 and L_1 absorption thesholds for the 3d transition metals. Evaluated from [39], except Sc and Zn [42].

dominated by a crystalline $CoSi_2$ phase [7, 32], *this demonstrates for the first time that an* in situ *determination of the local structure in buried layers is possible using EXAFS of the Co* $L_{2,3}$ *edges.*

We believe that L-EXAFS is a promising alternative to K-EXAFS for the investigation of these systems. Though the data analysis is more difficult in L-EXAFS for 3d TMs, the data is not distorted by Bragg diffraction beams as in the case of FY detected K-EXAFS. To overcome this difficulty in K-EXAFS, a complicated setup has to be used in order to selectively block the moving Bragg diffraction beams in front of the detector [32].

The same L-EXAFS technique as outlined above for Co should in principle be applicable to silicides formed by other 3d TMs. As listed in Table 2, the problems due to the superposition of the EXAFS oscillations due to L_3 and L_2 absorption channels are lower for the earlier 3d TMs due to the smaller spin orbit splitting. On the other hand, the L_1 edge is closer to the $L_{2,3}$ absorption threshold for the earlier 3d TMs. Consequently, the spectral region in which the influence of the polyspline is strong is extended.

In order to
(a) investigate early 3d TMs,
(b) improve the accuracy for the determination of the first shell distance,
(c) determine distances to the second and higher shells,
it is necessary to minimize the number of free parameters used to simulate the backgound due to the L_1 absorption. Thus it would be most favourable, if the shape of the L_1 absorption could be determined by an experiment.

The superposition of the $L_{2,3}$ EXAFS features is obviously a problem for such a measurement. However, if a process specifically related to the creation of an TM $2s$ core hole is chosen, the TM L_1 absorption could be selectively monitored. For buried samples this could be achieved by partially measuring the TM L_γ fluorescence radiation, generated by the radiative decay of the $2s$ core vacancy. As this radiation has to be separated from the much stronger TM L_α and L_β emission generated by the decay of the $2p$ core holes, this requires detectors with an energy

resolution better than 50 eV at 900 eV photon energy. Alternatively, the information concerning the L_1 absorption could be extracted from a non-buried sample by monitoring the Coster-Kronig decay of the TM 2*s* core vacancy.

4.1.4 Summary

In this section we presented L-EXAFS of 3d TMs as a new method to study the geometric structure of 3d TM silicides buried in a Si wafer. In contrast to K-EXAFS, this technique is easily compatible with the FY detection mode needed to investigate the buried structures *in situ*. The main problem for the data analysis in L-EXAFS is the superposition of the L_1 absorption features to the $L_{2,3}$ EXAFS oscillations. This problem can be overcome by accounting for this additional background by a polysplining procedure. The technique has been demonstrated for a buried $CoSi_2$ sample produced by IBS [7], where the first neighbour Co–Si distance could be determined as 2.32 ± 0.05 Å in good agreement with the $CoSi_2$ literature value of 2.323 Å [34].

4.2 FY-detection of XANES for concentrated samples

4.2.1 Introduction

The x-ray absorption near edge structure (XANES) in the soft x-ray region is in most cases monitored by electron yield (EY). Due to the limited escape depth of the electrons, the EY spectra do not reflect bulk properties but are largely dominated by surface effects. Though the escape depth can be varied in EY measurements by choosing an energy window in the partial yield mode, tedious sample preparations are necessary to minimize effects produced by adsorbates. For most materials even the clean surface contribution can not be neglected. This problem has been recognized *e.g.* in the study of high-T_C superconductors, where unambigious XANES results cannot be achieved using EY methods [46]. EY techniques are, for the same reason, not well-suited to study buried structures. Fluorescence yield (FY) detection has recently been introduced as a technique for the study of real bulk properties. As Jaklevic et al. [47] pointed out, this technique of recording x-ray absorption is especially useful in the investigation of dilute samples and thin layers. In these cases the FY signal is directly proportional to the absorption coefficient in question. Additionally, the signal-to-background ratio is higher in FY than in EY measurements of dilute samples and FY detection can easily be used in the presence of magnetic fields, *e.g.* in measurements of the magnetic circular dichroism. For concentrated bulk samples however, the measured FY is not proportional to the absorption coefficient. The experimental FY spectra exhibit distortions due to the so-called "self-absorption effects" [47, 48, 49]. These distortions vary with the geometry of the experiment. They are caused by the absorption of both the exciting photons on their way *into* the sample and the absorption of the generated fluorescence radiation on its way *out* of the sample.

The effect is illustrated in Fig. 24. In a grazing incidence geometry as shown in Fig. 24b, all incoming photons are absorbed close to the sample surface compared to the photon penetration length. Nearly all generated fluorescence photons will be able to escape out of the sample into the detector in a normal take-off setup, as their way through the sample is short compared to the penetration length. Consequently, if the electron transition investigated dominates the absorption, the signal is nearly independent of the absorption coefficient which we intend to measure in a XANES experiment. We note that all techniques that take advantage of a large escape depth to monitor bulk properties share this problem. As the spectrum appears to be saturated, this effect is somtimes adressed as "saturation effect" in FY spectra [48]. This is simulated in Fig. 25 for the Co $L_{2,3}$ edges.

In the normal incidence - grazing take-off limit as shown in Fig. 24c, however, the signal becomes more and more proportional to the absorption coefficient. The absorption of the generated fluorescence radiation on the way out of the sample attenuates the fluorescence radiation. If the absorption coefficient of the sample is high, most fluorescence radiation will be produced close to the surface, consequently the detected signal is high. If the absorption coefficient is low, a larger amount of the fluorescence is produced in deeper regions of the sample, thus contributing less to the detected signal.

So it is qualitatively clear that the saturation effects in the FY signal become weaker in

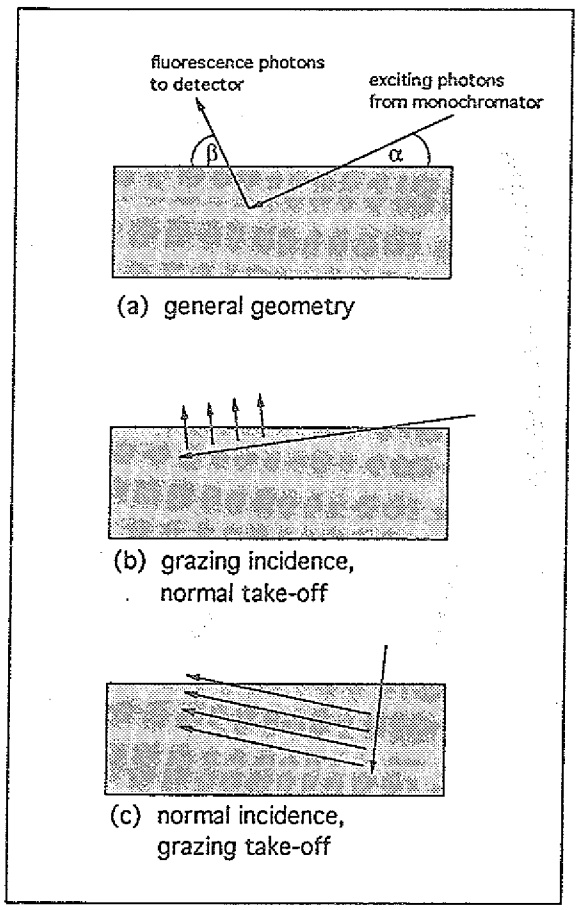

Figure 24: In this figure we illustrate the influence of the experimental geometry upon the saturation effects observed in the FY. (a) shows the general geometry: radiation from the monochromator enters the sample under the glancing angle α and may give rise to fluorescence radiation from the sample. The fluorescence radiation is detected under the angle β. In our setup $\alpha + \beta = 90°$. (b) shows the gracing incidence - normal take-off limit. Nearly all generated fluorescence photons contribute to the signal. If the electron transition investigated dominates the absorption, the signal is now nearly independent of the absorption coefficient of the sample and thus saturated. In the normal incidence - grazing take-off limit presented in (c), the signal becomes more and more proportional to the absorption coefficient *because* of the self-absorption experienced by the outgoing fluorescence photons, as fluorescence radiation generated deep in the sample can not reach the detector.

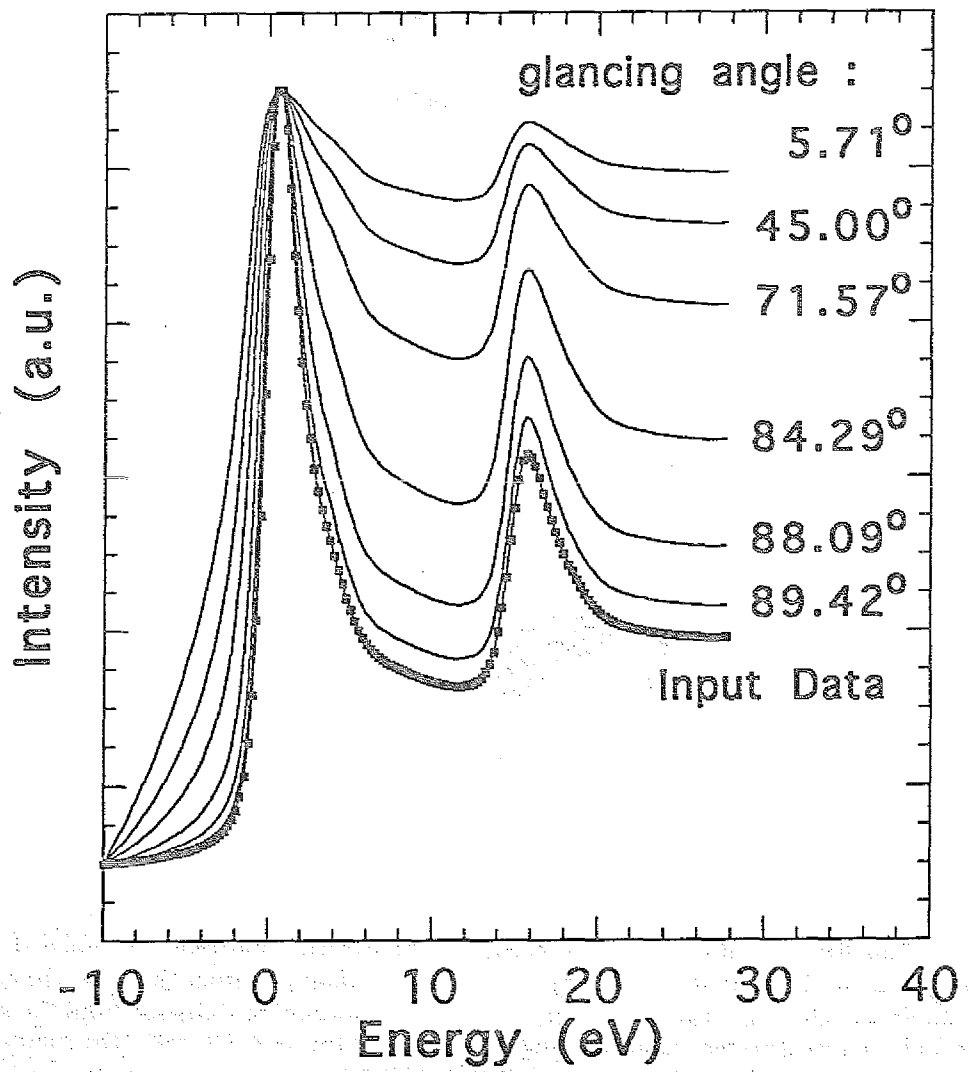

Figure 25: Simulation of equation (14), demonstrating the saturation effects observed in x-ray absorption spectra of concentrated samples detected by FY. The energy is measured relative to Co $2p_{\frac{3}{2}}$ electron binding energy. The calculations were carried out for Co using EY data as input (squares). It was assumed that $\mu_{other} = const. = \mu_{tot}(E_f)$, where the constant is 14% of the rise of the absorption coefficient over the $L_{2,3}$ edges [37, 51]. The intensities were calculated for geometry factors g of 0.1 (5.71°), 1 (45.00°), 3 (71.57°), 10 (84.29°), 30 (88.09°), and 100 (89.42°) and scaled to the L_3 peak for better comparison. See section 4.2.3 for a detailed discussion.

a normal incidence - grazing take-off geometry. However, we want to add that the term "self-absorption effect" used to explain the distortions in the grazing incidence FY spectra is misleading, as the *lack* of self-absorption produces saturation.

For the EXAFS energy range, the saturation effects can be corrected for using the information of the smooth background of the long dataset [36]. This is impossible on the short energy interval of interest in XANES. A normal incidence - grazing take-off geometry has been used to record XANES spectra as the saturation effects can be reduced in such a geometry [49]. However, in practice it is difficult to know whether the saturation effects are fully eliminated at the chosen geometry.

We report a different approach to determine the absorption of concentrated bulk samples by FY detection. As the absorption of the photons and the angular dependence can be described analytically, it is possible to determine the specific absorption coefficient of interest by analysing FY spectra recorded at different angles.

4.2.2 Theory

Consider a flat sample with thickness d oriented as shown in Fig. 24. Photons of energy E enter the sample with incident glancing angle α and can produce a core hole in a level X if their energy is sufficiently high. With the probability ω_X the hole decays by the emission of a photon with energy E_f. If the photon leaves the sample, it can be detected at take-off angle β by the detector with efficiency η. Let μ_X be the absorption coefficient associated with the production of a core hole in the investigated level X, $\mu_{tot} = \mu_X + \mu_{other}$ is the total absorption coefficient of the sample, while μ_{other} describes absorption due to shallower core levels, valence levels and other atomic species. The measured intensity is given by [47]:

$$I^X(E) = \eta \frac{A}{r^2} \omega_X I_0(E) \frac{\mu_X(E)}{\mu_{tot}(E) + \mu_{tot}(E_f)\frac{\sin\alpha}{\sin\beta}} \left[1 - e^{-\left(\frac{\mu_{tot}(E)}{\sin\alpha} + \frac{\mu_{tot}(E_f)}{\sin\beta}\right)d}\right] \quad . \tag{14}$$

$I_0(E)$ denotes the intensity of the incoming light, A is the active detector area and r the distance to the sample. The formula reflects the facts that the incident radiation is absorbed according to $\mu_{tot}(E)$ and that the absorption of the produced fluorescence radiation with the unique energy E_f is characterized by $\mu_{tot}(E_f)$. It is derived by integrating the law of absorption with the corresponding absorption coefficients over the paths of the photons through the sample. The variation of β due to the solid angle A/r^2 covered by the detector is assumed to be small.

Thick samples are characterized by

$$e^{-\left(\frac{\mu_{tot}(E)}{\sin\alpha} + \frac{\mu_{tot}(E_f)}{\sin\beta}\right)d} \ll 1 \quad , \tag{15}$$

i.e. the sample is thick with respect to the photon penetration depth. In this limit the exponential term can be neglected and the measured intensity is given by

$$I^X(E) = \eta \frac{A}{r^2} \omega_X I_0(E) \frac{\mu_X(E)}{\mu_{tot}(E) + \mu_{tot}(E_f) g} \quad . \tag{16}$$

The spectra are angle dependent via the geometry factor $g := \sin(\alpha)/\sin(\beta)$. Thus, if measurements are carried out at different geometries g_1 and g_2, different spectra $I_1^X(E)$ and $I_2^X(E)$ will be observed. Using the normalized experimental spectra $I_i(E) := I_i^X(E)/I_{0i}(E)$ and $c_i^{-1} := \eta\frac{A_i}{r_i^2}\omega_X$ the two spectra can be described as

$$I_1 = c_1^{-1}\frac{\mu_X(E)}{\mu_{tot}(E) + \mu_{tot}(E_f)g_1} \quad \text{and} \tag{17}$$

$$I_2 = c_2^{-1}\frac{\mu_X(E)}{\mu_{tot}(E) + \mu_{tot}(E_f)g_2} \quad . \tag{18}$$

These equations can be solved for the absorption coefficients:

$$\mu_{tot}(E) = \mu_{tot}(E_f)\frac{g_2c_2I_2(E) - g_1c_1I_1(E)}{c_1I_1(E) - c_2I_2(E)} \quad \text{and} \tag{19}$$

$$\mu_X(E) = \mu_{tot}(E_f)(g_2 - g_1)\frac{c_1I_1(E)\,c_2I_2(E)}{c_1I_1(E) - c_2I_2(E)} \quad . \tag{20}$$

By determining the quantities $I_i(E)$, g_i and c_i the the absorption coefficients can be evaluated relative to $\mu_{tot}(E_f)$. $I_i(E)$ and g_i are directly measurable, and below we will discuss how the uncertainty in c_i can be taken into account.

Note that in eqn. (20), the geometry factors g_i are only scaling the spectrum and do not affect its shape. This means that one does not have to accurately determine the geometries. Any two spectra recorded at different angles will produce the same μ_X-*shape* as evaluated by eqn. (20). However, as the information depth changes as a function of the angle, for inhomogenous samples two geometries corresponding to the same information depth should be chosen. This is discussed in more detail in section IV. It must also be noted that it is helpful to choose geometries resulting in two significantly different experimental spectra to minimize errors due to the denominator of eqn. (20). A second advantage of eqn. (20) is that it is valid not only on the high energy side of an absorption edge, but also below the edge. If the photon energy is lowered below the threshold value, all measured intensities drop to zero. While eqn. (19) is no longer defined in this limit, eqn. (20) still holds, as the numerator approaches zero quadratically in contrast to the denominator.

In the case where $c_1 = c = c_2$, equation (20) can be written as

$$\mu_X(E) = \mu_{tot}(E_f)(g_2 - g_1)c\,\frac{I_1(E)\,I_2(E)}{I_1(E) - I_2(E)} \quad , \tag{21}$$

i.e. the shape is neither affected by the geometry factors g_i nor by the proportionality factor c.

However, it can be experimentally difficult to fulfill the condition $c_1 = c_2$. If that is not possible, c_1 and c_2 have to be determined in order to use the expressions (19) and (20).

This problem can be solved by using assumptions about μ_{other}. If the level of interest X is separated far enough in energy from adjacent core levels, it is a good approximation to use $\mu_{other} = const.$ on the narrow energy range of interest in XANES. If one can further assume that all the emission falls below the absorption edge, this constant equals $\mu_{tot}(E_f)$:

$$\mu_{tot}(E) = \mu_X(E) + \mu_{tot}(E_f) \quad . \tag{22}$$

Using eqns. (19) and (20), eqn. (22) can be rewritten as

$$c_1 = [I_2(E)(1+g_2) - \frac{c_1}{c_2} I_1(E)(1+g_1)]/[I_1(E)I_2(E)(g_2-g_1)] \quad . \tag{23}$$

As c_1 and c_2 must be independent of energy, this equation can be used to determine these factors. The ratio c_1/c_2 has to be varied as a parameter until c_1 is constant as a function of energy.

Using this method, it is easy to evaluate $c_{1,2}$ with sufficient accuracy so that the formulas (19) and (20) can be used to determine the absorption coefficients. It must be noted, that this procedure depends on the determination of the correct values for g_i.

4.2.3 Results and Discussion

In this section we will demonstrate the technique to derive the absorption coefficient described in the previous section. Using polished and sputtered Co metal as sample, we can compare the results to EY data. Additionally, the information depth of the method is analysed.

To illustrate the effects associated with self-absorption in the fluorescence yield detection of XANES for concentrated samples, Fig. 25 shows a simulation of the basic equation (16) for Co, in the experimental geometry described above, using EY data as input for μ_X. $\mu_{tot}(E_f)$ was estimated to be 14% of the total rise of the total absorption coefficient over the $L_{2,3}$ edges [37, 51] and the validity of eqn. (22) was assumed. As the total intensity decreases with increasing glancing angle, the calculated FY spectra and the EY input data have been scaled to the L_3 edge jump in Fig. 25. Besides the fact that the overall signal gets more intense in grazing incidence, the main effect of the self absorption is to enhance low-signal regions of the spectrum under the grazing incidence conditions. As high-signal regions of the spectrum are less enhanced, the spectral features are more and more "washed out" if a more grazing incidence setup is chosen. Thus the spectrum appears to be saturated. The absorption edge is broadened due to this enhancement of low signal regions and appears to be shifted to lower energies for lower g values. Consequently it is of utmost importance to correct for these effects when electron binding energies are to be determined.

For g $\rightarrow \infty$, which corresponds to a normal incidence and grazing take-off geometry, the FY signal approaches the real absorption spectrum, a fact which has been used to record FY-spectra [49]. This is always true, if $(\mu_{tot}(E_f)\, g)$ dominates the denominator of eqn. 14. If on the other hand $\mu_{tot}(E) \gg (\mu_{tot}(E_f)\, g)$, the saturation effect can still be small if $\mu_{tot}(E) \gg \mu_X(E)$. This condition defines the dilute sample limit, where μ_{other} is high due to the presence of other atomic species. The smaller μ_{other} gets, the stronger is the saturation effect in the FY spectra, leading to a completely saturated signal in the extreme case where $\mu_{tot}(E) = \mu_X(E)$. Thus a geometry characterized by a sufficiently high g has to be chosen to monitor the absorption if the data is not corrected for these effects. Then, however, count rates are lower due to the strong self-absorption and the information depth will get smaller as we will see below.

In Fig. 26 experimental data for the Co L_3 absorption edge of a polished and sputtered Co sample are shown, demonstrating the effect of self-absorption in the FY spectra. Two FY spectra recorded at different geometries are compared to the EY signal. Because of the small escape depth even for inelastically scattered electrons, the EY signal can be assumed to be proportional to the absorption coefficient of Co. The prominent peak visible can be related to the density of unoccupied electronic states of d symmetry at the Co atom.

The calculated self-absorption effects as presented in Fig. 25 are clearly visible in the experimental spectra. The grazing incidence (glancing angle $\alpha = 27.0°$, g = 0.51) FY spectrum differs clearly from the EY spectrum. The pre-edge signal is enhanced resulting in a broadening of the peak and an apparent shift of the edge. In contrast to the real absorption coefficient, the intensity does not drop significantly on the high-energy side of the absorption edge. In the normal incidence (glancing angle $\alpha = 85.0°$, g = 11.4) FY spectrum the saturation effects smaller, but the signal is still not proportional to the absorption coefficient as measured by total EY, demonstrating the need to correct for the angular dependence of the FY spectra.

The two FY spectra as shown in Fig. 26 have been used to calculate the total absorption coefficient $\mu_{tot}(E)$ and the absorption coefficient $\mu_{L_3}(E)$ assocciated with the production of the Co $2p_{\frac{3}{2}}$ core hole using eqns. (19), (20) and (23). The results are shown in Fig. 27. The absorption coefficients are plotted in units of the total absorption coefficient below the L_3 threshold $\mu_{tot}(E_f)$. As expected, the two spectra differ only by an additive constant. As this behaviour was assumed by using eqns. (22)–(23) to determine the constants c_i, this demonstrates the self-consistency of the procedure.

Note that $\mu_{tot}(E)$ calculated according to eqn. 19 is more influenced by the uncertainties of the two input data sets than $\mu_{L_3}(E)$. As pointed out in a previous section, equation (19) used to calculate $\mu_{tot}(E)$ is not well-defined below the absorption threshold, consequently the plotted $\mu_{tot}(E)$ curve is not correct in this energy range. This results in a large variation and an incorrect offset of the $\mu_{tot}(E)$ curve relative to $\mu_{L_3}(E)$ in the pre-edge region. Nevertheless, if the post-edge offset of the two absorption coefficients is used, the pre-edge value of the total absorption coefficient can be determined approximately as $\mu_{tot}(E = 771eV) \simeq \mu_{tot}(E_f)$, again demonstrating the self-consistency of the analysis. It can be estimated that $\mu_{tot}(E)$ increases by a factor of 4.5 ± 1.5 when the energy is varied over the Co L_3- *and* L_2-edges, which is slightly lower than other values reported [37, 51, 38].

The *absolute* values of the absorption coefficients calculated in this way depend on a correct determination of the experimental geometry. In our measurements the angle of incidence was determined to an accuracy of 1°. The uncertainty in the take-off angle due to the acceptance of the detector was 10° for the closest detector position. We estimate the resulting error for the determination of absolute values of the absorption coefficient to be about 50%.

However, in most experiments relating the XANES to the electronic structure the correct *shape* of the absorption coefficient is of primary importance. Thus the derived $\mu_{L_3}(E)$ absorption coefficients will be used in further discussions, because

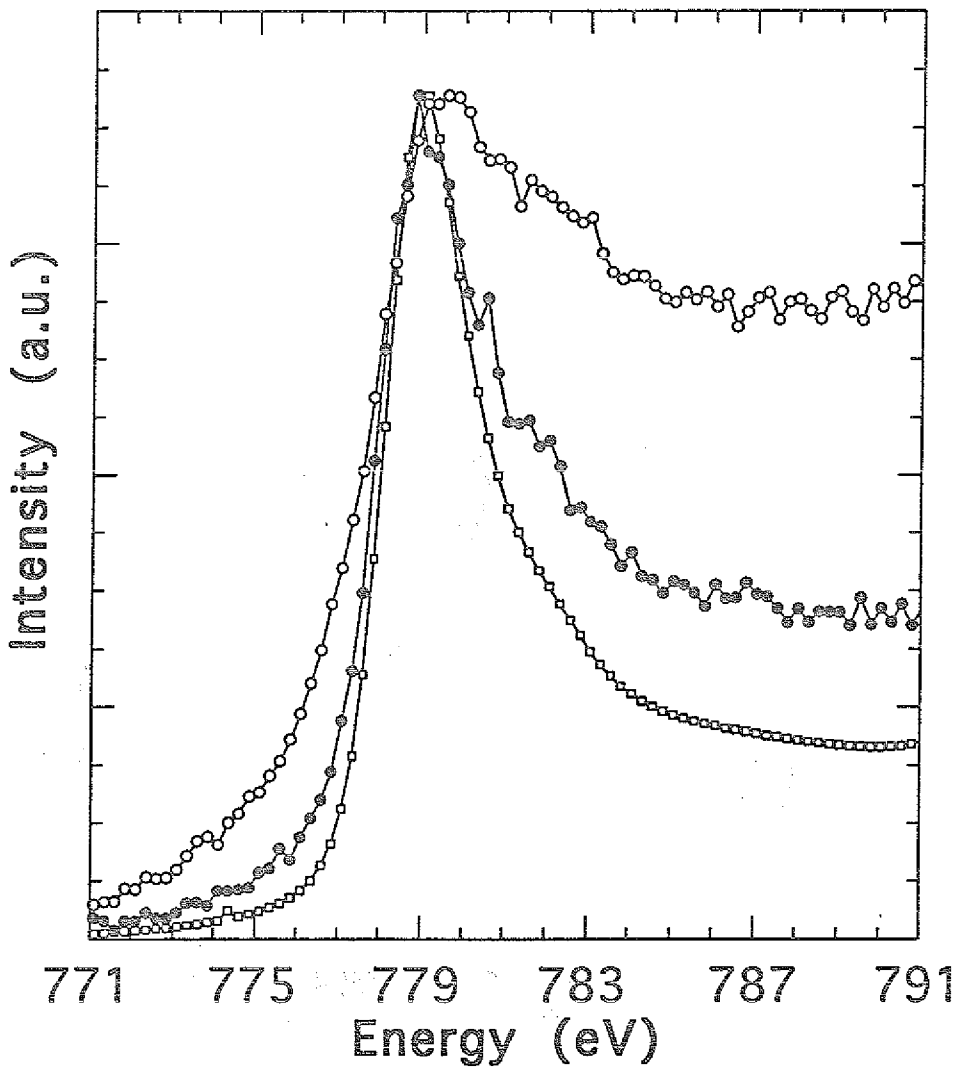

Figure 26: Co L_3 XANES as detected by EY (squares) and FY (circles) as a function of photon energy. Intensities have been normalized to the L_3 peak. FY spectra have been recorded for two different experimental geometries: glancing angle of incidence 27.0° (open circles) and 85.0° (filled circles). Strong saturation effects are present in the 27.0° spectrum: low-signal regions appear to be enhanced. The saturation effects are reduced in the 85.0° geometry but are still distorting the shape of the spectrum, as indicated by comparison with the EY data.

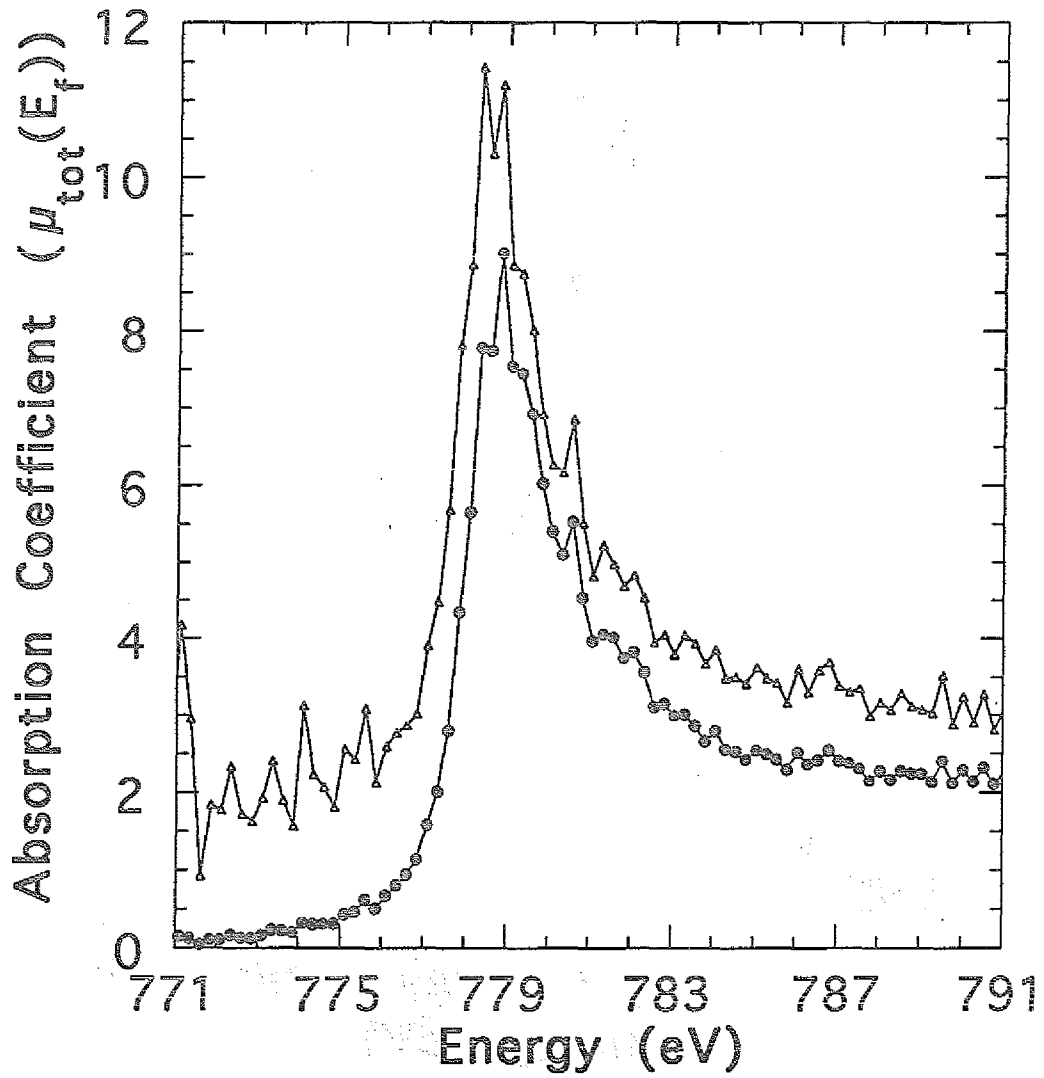

Figure 27: Total absorption coefficient μ_{tot} (open triangles) and the absorption coefficient associated with the creation of a Co $2p_{\frac{3}{2}}$ core hole μ_{L_3} (filled circles) as a function of photon energy. One unit on the y-axis corresponds to the total absorption coefficient at the fluorescence photon energy E_f. The spectra have been calculated from the FY data in Fig. 26 using eqns. (19), (20), and (23).

(a) this is the physical property of interest with respect to the electronic structure determination in XANES,
(b) $\mu_{L_3}(E)$ as determined by eqn. (20) is well-defined over the whole energy range and
(c) it is not as as sensitive on the statistical scattering of the input data as $\mu_{tot}(E)$.

In Fig. 28 the FY derived $\mu_{L_3}(E)$ for Co is compared to the EY signal. In comparison with the uncorrected normal incidence FY spectrum presented in Fig. 25 the improvement is obvious: $\mu_{L_3}(E)$ as derived from the angular dependence of the FY as outlined above fits very well to the EY spectrum, supporting the validity of the analysis method. Both the L_3 edge position as well as the overall shape are reproduced, when the error due to the statistics and the determination of the geometry factors are taken into account (see Fig. 29).

The uncertainty due to the angle measurement is quantified in Fig. 29. The solid lines represent the derived absorption coefficients, if the angle of incidence is $\pm 1°$ off the value used for the dotted spectrum. Even for a detector position close to the sample, the error due to the detector acceptance angle is slightly smaller. It could be reduced by placing a slit in front of the detector in future experiments.

Note that this angular dependence is not given by equation (20) itself. It enters indirectly via the use of eqn. (22) to determine the proportionally factors $c_i := (r_i^2)/(A_i \eta \omega_{L_3})$ in the two FY spectra as described in the theory section. This method is illustrated in Fig. 30 showing the value c_1, the constant of proportionality for the grazing incidence FY spectrum, after the parameter c_1/c_2 has been varied to find the best value characterized by the condition $c_1(E) = const.$. This condition is clearly fulfilled in the energy range above 779 eV, *i.e.* above the absorption coefficient peak energy, allowing us to determine c_1 and c_2 with sufficient accuracy. The possible error due to this method is estimated to be smaller than the consequences of an errounous angle determination as depicted in Fig. 29. The scattering of c_1 on the low energy side of the L_3-absorption threshold ($E < 776eV$) indicates the fact that eqn. (22) is not well-defined in this energy range as mentioned above. It is impossibe to find a parameter c_1/c_2 in such a way, that c_1 is constant between 776 eV and 779 eV. We do not have an unambiguous explanation for this observation.

We will now investigate the information depth of the technique. The probability to detect a fluorescence photon generated in the depth x perpendicular to the surface is described by

$$P(x) \propto \exp[-(\frac{\mu_{tot}(E)}{\sin\alpha} + \frac{\mu_{tot}(E_f)}{\sin\beta})x] \quad . \tag{24}$$

The information depth λ_f of the FY detection can be defined as the expectation value of x with respect to this probability distribution [36]:

$$\lambda_f := \frac{\int_0^\infty x P(x) \mathrm{d}x}{\int_0^\infty P(x) \mathrm{d}x} \tag{25}$$

$$= \frac{\sin\alpha}{\mu_{tot}(E) + \mu_{tot}(E_f) g} \quad . \tag{26}$$

Figure 31 shows the information depth for pure Co as a function of the glancing angle α (see Fig. 24, $\alpha + \beta = 90°$) for two different energies. The information depth is limited by the absorption

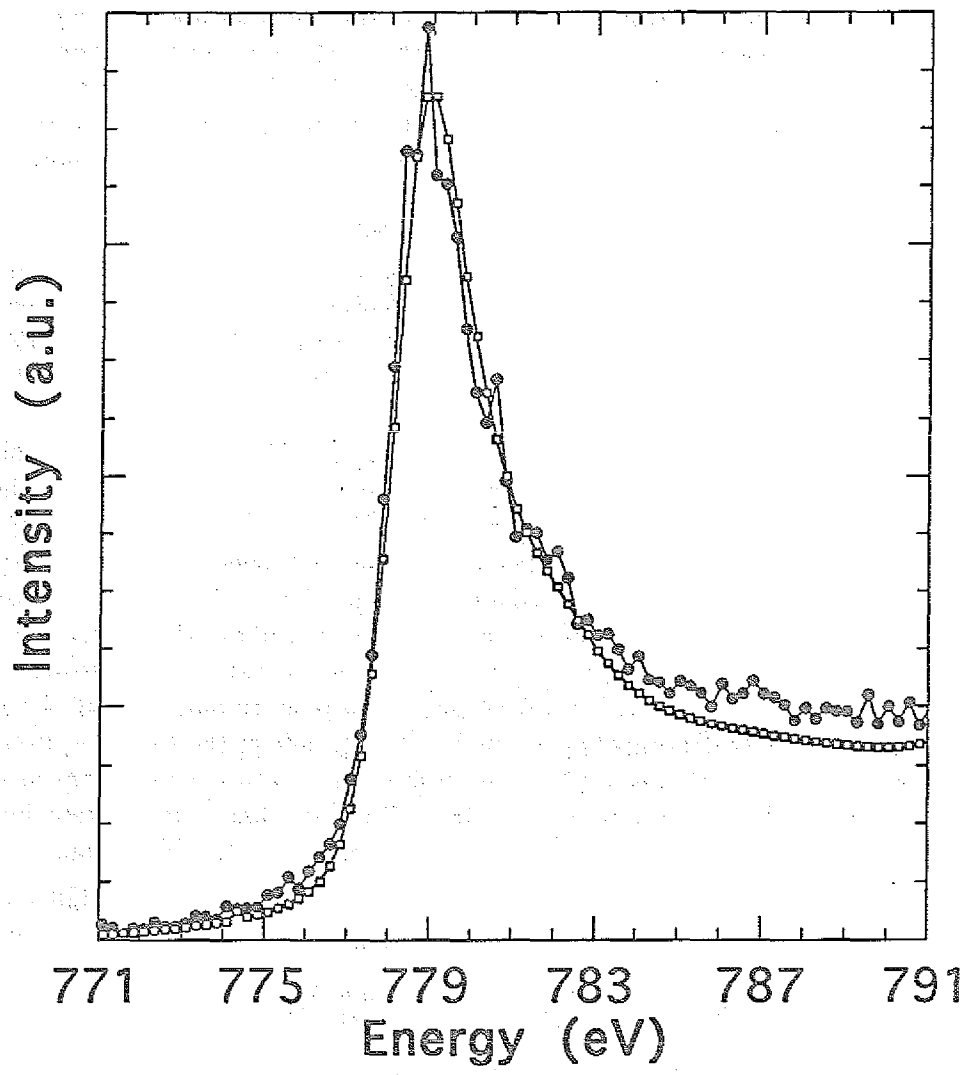

Figure 28: Co L_3 XANES spectrum derived from the FY measurement (filled circles) as presented in Fig. 27 compared to the EY spectrum (open squares). The FY derived spectrum is in good agreement with the EY spectrum, when the uncertainty due to the statistics and the determination of the experimental geometry as presented in Fig. 29 is taken into account.

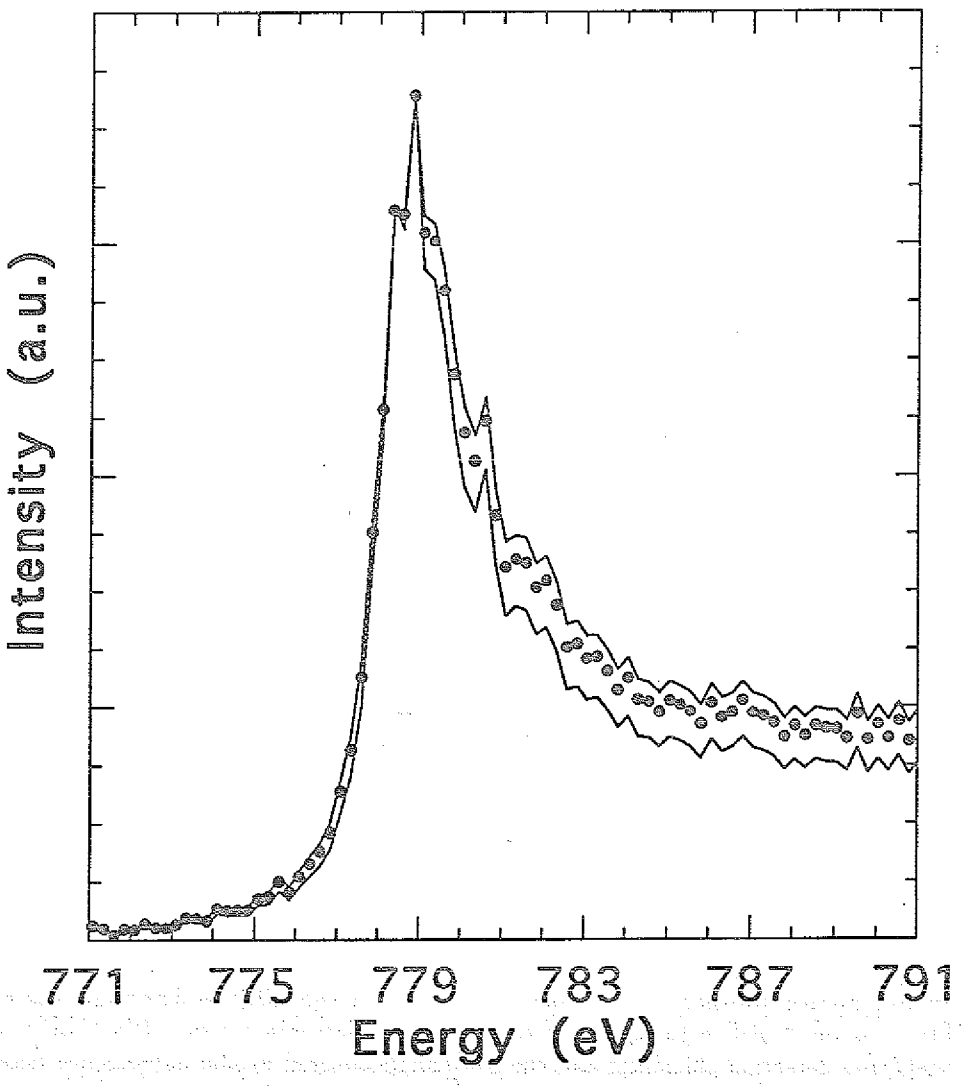

Figure 29: In this figure we illustrate the influence of an erroneous determination of the experimental geometry on the shape of the derived XANES spectrum. The solid lines represent the absorption coefficients derived, if the angle of incidence is $\pm 1°$ different from the value used for the calculation of the dotted spectrum. The additional error due to the finite detector acceptance was found to be slightly smaller than the indicated error due to the determination of the incidence angle.

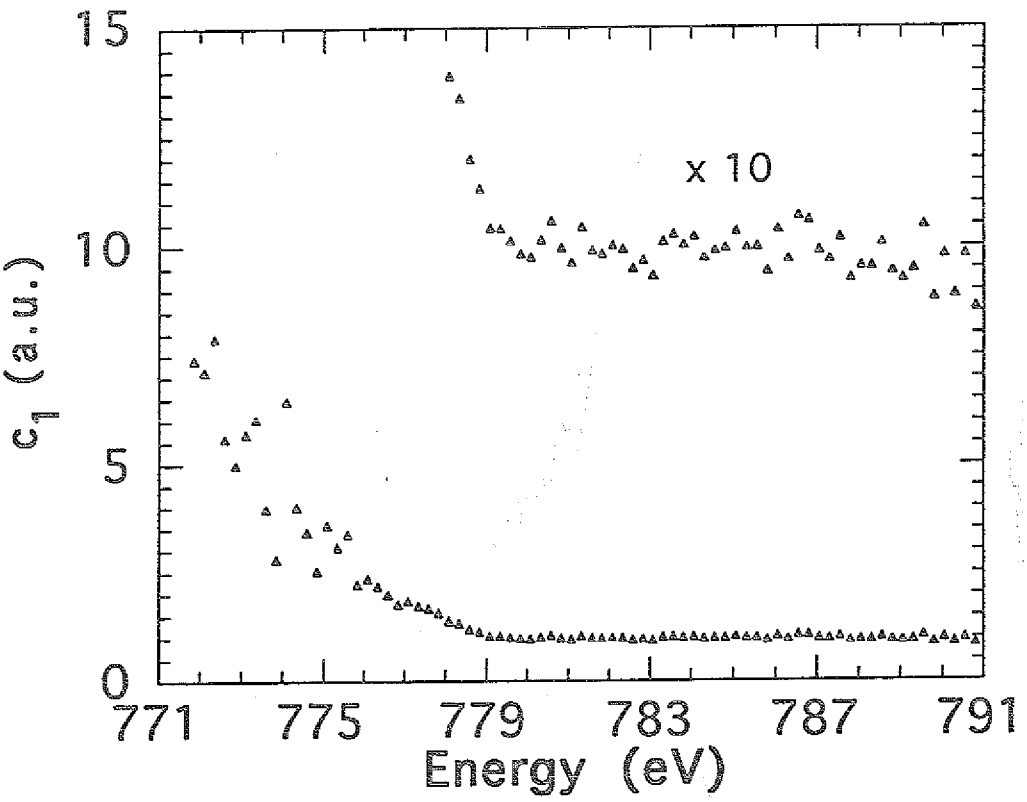

Figure 30: In this picture we illustrate the method relying on eqn. (23) to determine the constants of proportionallity c_i as described in the theory section. These constants are inversely proportional to the fluorescence yield, the detection efficiency, and the solid angle covered by the fluorescence detector. They have to be determined in order to calculate the absorption coefficient from the two FY spectra recorded at different angles. For the Co system, the c_1 value corresponding to the grazing incidence spectrum is shown as a function of photon energy, after the parameter c_1/c_2 has been varied according to eqn. (23) to fulfil the condition $c_i(E) = const.$. See text for a more detailed discussion.

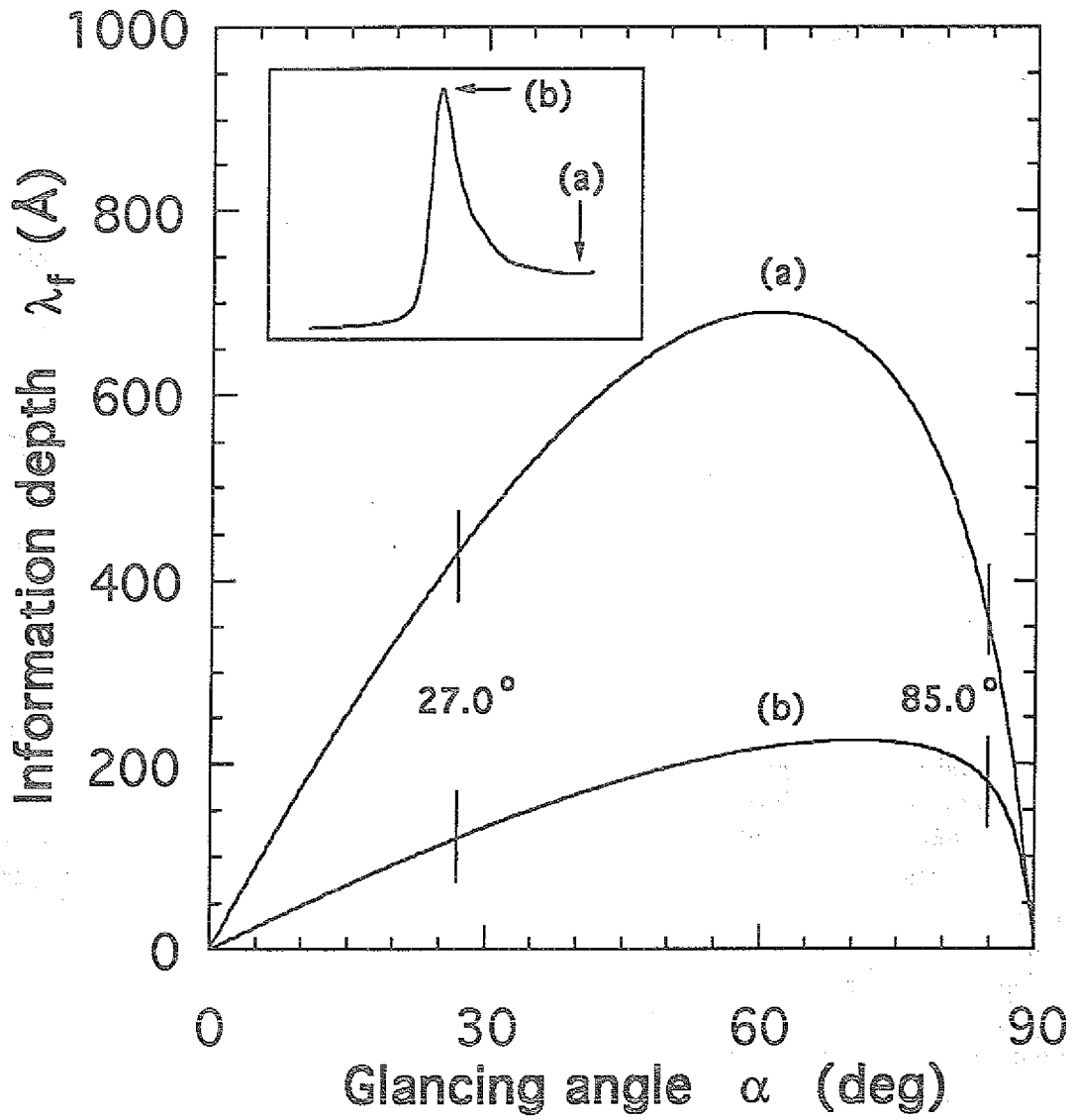

Figure 31: This figure shows the information depth λ_f as a function of the angle of incidence for Co in our experimental setup ($\alpha + \beta = 90°$). The information depth varies with photon energy due to the variation of the absorption coefficient over the Co L_3 edge shown in the inset. Thus the information depth has been calculated for the maximum absorption (b) and for an absorption value above the L_3 edge (a). The angles of incidence chosen for the two FY spectra to derive the Co XANES are indicated (see Fig. 26).

of the generated fluorescence photons for glancing angles close to 90° and by the absorption of the incident photons for small glancing angles. Consequently, the information depth has a maximum at intermediate angles. The asymmetry is caused by the fact that $\mu_{tot}(E_f)$ is smaller than $\mu_{tot}(E)$, if the energy E is above the absorption edge.

As $\mu_{tot}(E)$ shows a strong variation in the XANES region (inset in Fig. 31), the information depth is energy dependent. Curve (a) shows the information depth for an energy 13 eV above the absorption edge while (b) shows the information depth at the energy corresponding to the strongest absorption.

For the first case, the information depth maximum of about 700 Å is obtained for a glancing angle of about 60°. In the second case, the information depth is considerably reduced to a maximum value of 225 Å, peaking at 70°. Thus one has to be aware that the information depth changes as a function of $\mu_{tot}(E)$ while scanning a XANES spectrum of a concentrated sample in the FY detection mode.

In order to derive the absorption coefficient as outlined in the theory section, two measurements at different angles have to be made. Due to shape of the information depth as a function of the glancing angle, it is always possible to choose two geometries which correspond to the same information depth. The angles used for the measurements on Co presented above are indicated in Fig. 31. They correspond to a maximum information depth of about 400 Å ((a)) and a minimum information depth of about 175 Å ((b)). Thus we are bulk sensitive in our measurements.

For the buried structures like the IBS $CoSi_2$ layer described in section 3.2, the information depth calculated in this way starts at the beginning of the buried layer. As no Si absorption edges are present in the energy range investigated, the Si absorption can be regarded as constant over the spectral energy range. Additionally, there is no contribution to the fluorescence signal originating from this Si cap layer.

Thus, the influence of the silicon cap layer can be described as simply reducing the incident photon flux and the detection efficiency for the fluorescence photons. Consequently, the spectral shape remains unaffected by the cap layer, only the intensity is reduced. This reduction can be calculated if the thickness of the cap layer is known. However, this intensity scaling is automatically accounted for if the proportionallity factors c_i are determined using eqn. (23) as described in section 4.2.2.

We will apply the technique presented above to a buried $CoSi_2$ layer in section 5.

4.2.4 Summary

We presented a new method to determine the absorption coefficient in the XANES energy range for concentrated samples by monitoring the fluorescence yield. The method uses the fact that it is possible to describe the angular dependence of the absorption processes occuring in this photon-in photon-out type of spectroscopy analytically.

Making measurements at two different experimental geometries, it is possible to calculate the absorption coefficient. Thus we are able to correct for the saturation effects often present in FY derived spectra of concentrated samples. The technique was demonstated for a pure Co sample.

The information depth of the method was investigated and found to be large enough to

measure real bulk properties of the sample. By FY detection, it is possible to study buried layers which are unaccessible by conventional electron spectroscopies.

5 Electronic Structure of Cobalt Disilicide

5.1 Introduction

In this section we present an investigation of the electronic structure of $CoSi_2$.

We have studied buried layers of $CoSi_2$ in Si using Fluorescence Yield Soft X-ray Absorption (FY-SXA) and Soft X-ray Emission (SXE) spectroscopy .

The local, atom-specific nature of the x-ray processes make them ideal to study buried structures, *e.g.* the local electronic structure around buried Co atoms in a Si matrix. It is well-known that the behavior of the metal *d*-derived bands are important for the electronic properties and the bond formation in the silicides, and we have here, via transitions involving the Co $2p_{\frac{3}{2}}$ electrons, studied the occupied and unoccupied Co *d*-DOS in buried layers of $CoSi_2$.

There have been some XANES spectra of transition metal disilicides presented in the literature [54, 61], and recently also Co L absorption spectra of $CoSi_2$ have been measured [61, 58]. Here we present a Co L_3 electron yield (EY-) XANES spectrum of a $CoSi_2$ single crystal with a considerably improved resolution that allows for a detailed comparison to theory. For the ion beam synthesized buried structures conventional EY-SXA spectroscopy can not be used, since the secondary electrons are absorbed in the Si cap layer. We have used the FY technique, taking advantage of the large penetration depth of the soft x-rays.

Transition metal silicides have been studied in SXE [52, 53, 54, 55], and also a transition metal L emission spectrum has been measured [55]. We here present a spectrum that allows us to make a more detailed comparison with theory, and we show that local Co *d*-DOS, obtained via the SXE spectrum, can be measured directly on a buried ion beam synthesized $CoSi_2$ layer.

By combining the two spectroscopies we get a complete picture of the Co *d*-DOS in $CoSi_2$, especially we refer the various DOS features to the Fermi level, providing a test for band structure calculations.

5.2 Electronic structure of TM silicides

The forming of chemical bonds and the electronic structure in 3*d*, 4*d*, and 5*d* TM silicides in general is often discussed using the simple scheme presented in Fig. 32 in terms of directed valence orbitals [56, 57, 58, 59, 60].

Imagine the formation of a TM silicide starting from the pure TM by inserting Si atoms into the metal lattice. The most prominent feature in the TM electronic structure is the *d* band formed by the individual d orbitals. When Si is inserted, the *d* orbitals are driven farther from each other, resulting in a smaller TM *d*–TM *d* overlap. As a concequence, the *d* bonding strength is lowered and the *d* band narrows. These TM *d* orbitals directed to neighbouring TM atoms only take limited part in the TM–Si bonding and are addressed as nonbonding. Those TM *d* orbitals directed towards neighbouring Si atoms interact with the Si *p* orbitals resulting in bonding and antibonding states energetically below and above the nonbonding states, respectively.

This scheme is meant to describe the main features of the TM silicide electronic structure. As a lot of different TM silicides with various stoichiometries ranging from $TMSi_3$ to TM_3Si exist,

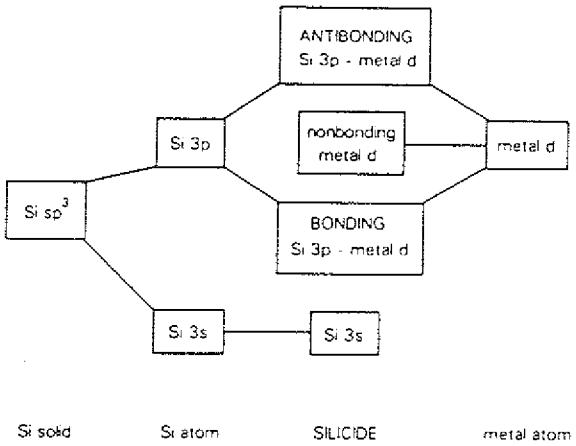

Figure 32: Schematic picture of the formation of the TM silicide electronic structure (from Ref. [56]).

it can not be expected that this picture describes every system in detail. For $CoSi_2$ and $NiSi_2$ it has been shown that this simple p–d bonding model is not sufficient to describe the electronic structure. For these disilicides the Si orbitals are sp^3 hybridized and sp^3–d hybridization was found to be important [53].

Furthermore, it is essential for an understanding of the electronic structure to locate the Fermi energy in the diagram shown in Fig. 32. In this simple picture it rises with the growing TM d shell occupancy in a given TM row of the periodic system.

The DOS emerging in the silicide formation is shown schematically in Fig. 33. The effect of the TM d–Si p coupling is to spread out the TM d band over a larger energy range compared to the pure TM, although the nonbonding part of the band is narrower than the pure TM d band. In the Si sp band, weight is pushed towards the the bonding and antibonding regions above and below the nonbonding states.

In Fig. 34 calculated DOS for $CoSi_2$ is shown [60]. The features discussed in the context of the general scheme can be observed in the total DOS (solid line) and partial d DOS at the Co atom (dashed line). Though $CoSi_2$ is metallic, there is a region of low DOS in the vicinty of the Fermi energy. This region between the nonbonding and the antibonding states is often addressed as 'quasi-gap'.

5.3 Results and Discussion

5.3.1 DOS information from soft x-ray spectra of $CoSi_2$

The identification of structures in the soft x-ray spectra with structures in the DOS predicted by band structure calculations are often straightforward (See section 2.2). We argue here that it is also justified to assume that the Co L XANES and SXE spectra measure the Co d-DOS in cobalt silicides.

The matrix elements determine the intensity ratio between s and d states in the L spectra. In the Co $2p$ to conduction band transitions the d states are totally dominating and we therefore neglect the s-DOS in our interpretation of the spectra. The matrix elements vary smoothly with

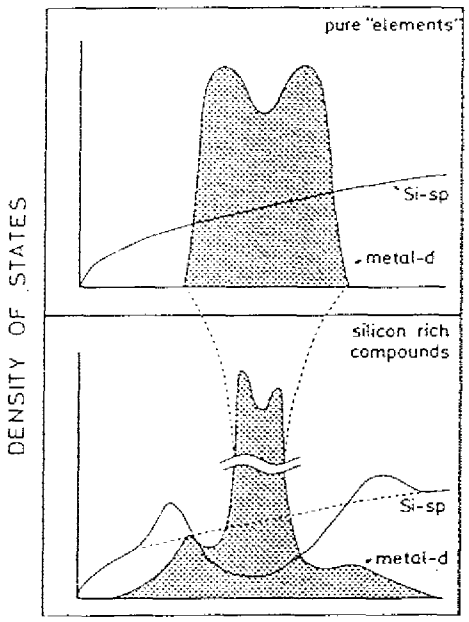

Figure 33: Schematic DOS diagram for pure Si and TM (top) and a TM silicide (bottom). In the silicide, the former TM d band narrows to the nonbonding states. Bonding and antibonding states evolve above and below this region due to the TM–Si interaction. Consquently, Si *sp* weight is pushed to this regions as well resulting in a low *sp* DOS in between. (From Ref. [57], modified)

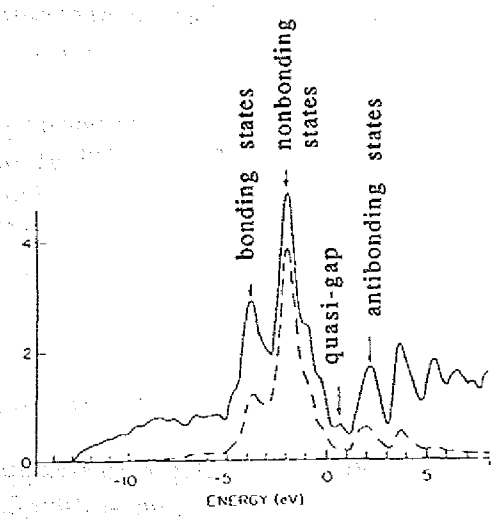

Figure 34: $CoSi_2$ DOS as calculated by Tersoff and Hamann [60]. Solid line: total DOS; dashed line: partial *d* DOS at the Co site.

energy without adding any structure to the spectrum [61]. Especially when the features of interest are located within a small energy range no attention has to be paid to the matrix element energy variation.

Inherent broadening comes from the finite lifetimes of the initial and final states. The core hole lifetime width is probably close to the value for elemental Co, 0.32 eV [62]. The lifetime of the valence hole in SXE and of the excited electron in XANES varies from negligible at the Fermi level to 1-2 eV further away in the band, causing an extra smearing at the corresponding transition energies. Since we are interested in structures close to the Fermi level this broadening should not be important. Phonon broadening can probably be neglected in this case.

The forming of the $CoSi_2$ band fits into a simple scheme described in section 5.2 that has been used to understand the behavior of TM silicides in general [57].

We expect distortions due to excitation-emission dynamics and electron correlation to be small, on the basis of this general discussion of the overall band structure.

For strongly correlated systems the one-electron interpretation of the SX spectra presented above is of course erroneous. For such systems the spectra are better described in terms of quasi-atomic excitations [63]. Here the excitations in XAS largely involve the highly dispersed antibonding Co d-Si sp^3 levels, where no quasi-atomic model can give a good description of the excitations. If correlation at all plays a role we expect it in the localized nonbonding states. This could have some impact on the SXE spectrum, which we will discuss later.

In free electron-like systems one gets additional structure due to the interaction between the electron gas and the core levels [19] as outlined in section 2.2.2. The presence of the narrow nonbonding bands in $CoSi_2$ suggests that free-electron like response should be negligible in our case. Also, the DOS close to the Fermi level, where the largest effects are expected, is relatively small in $CoSi_2$.

According to the final state rule [14] the SXE spectrum should directly correspond to the local ground state DOS, whereas the local DOS with the core hole potential should be compared with the XANES spectrum. We will come back to this point when discussing this spectrum.

5.3.2 The Unoccupied Co d-DOS of $CoSi_2$

We will first discuss the total EY Co L_3 absorption spectrum of single crystal $CoSi_2$ (see Fig. 35). We established the energy scale by direct comparison with the EY of Co metal[10], and aligning the spectrum to the Co Electron Energy Loss Spectroscopy (EELS) data of Fink *et al.* [64]. The $CoSi_2$ spectrum shows a clear Fermi cut-off at the low energy side, as expected for a metallic system. In Fig. 35 we have used the inflection point of the sharp edge to refer the spectrum to the Fermi level. The subtracted energy, which we take as a measurement of the $2p_{\frac{3}{2}}$ binding energy, is 779.0 eV, in agreement with the XPS value, 778.9 eV [65]. The inflection point in the XANES spectrum of pure Co metal is at 778.3 eV, also close to peak values measured in direct photoemission [65, 39]. The core level shift (0.7 eV) for $CoSi_2$ relative to metallic Co is, however, larger than the 0.4 eV XPS shift [65]. In XPS the uncertainty originates from the asymmetry of

[10]The spectra were recorded in the same injection.

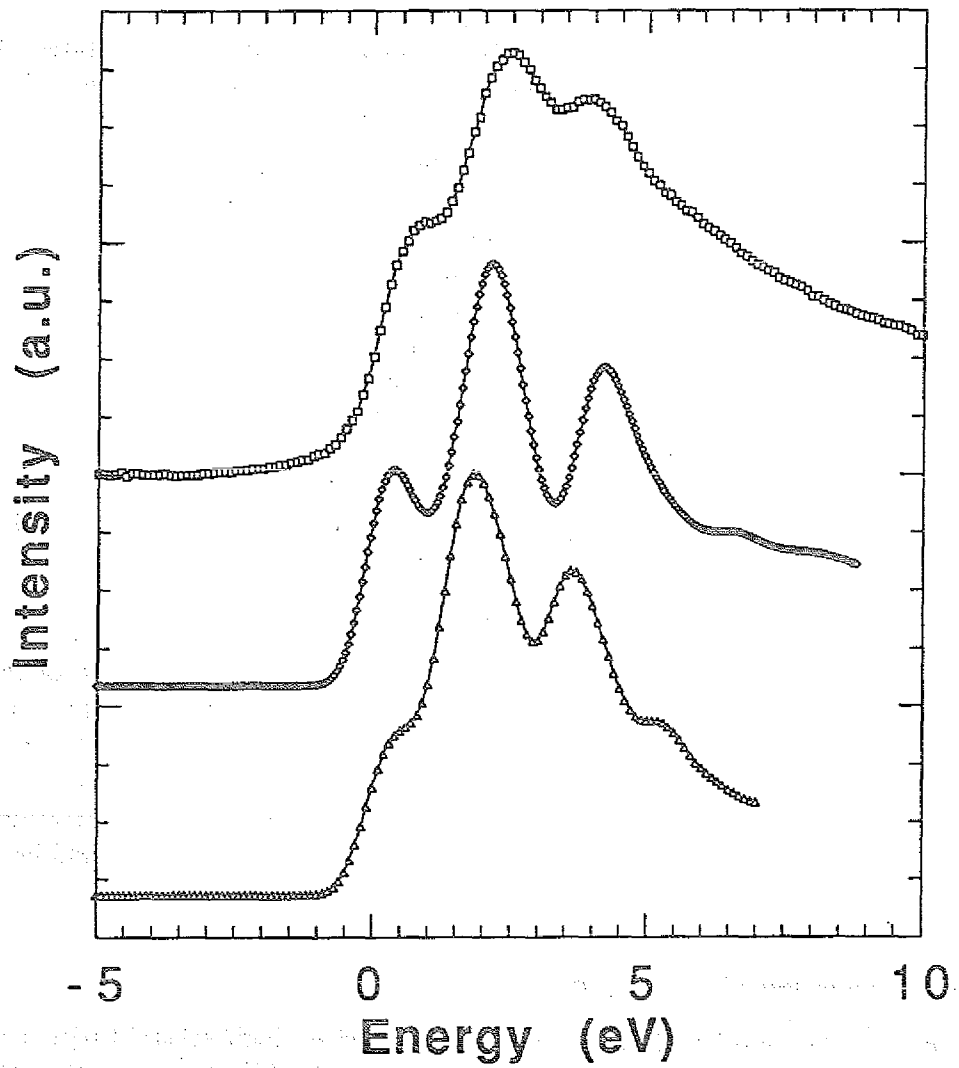

Figure 35: The upper curve (squares) is the Co L_3 total electron yield spectrum of a $CoSi_2$ single crystal, measured with 0.7 eV resolution and referred to the Fermi level using the inflection point of the edge. The middle curve (diamonds) is the projected Co *d*-DOS according to van Leuken [70] and the lower curve (triangles) according Tersoff and Hamann [60]. Both curves are convoluted with a gaussian of 1.0 eV FWHM.

the peak, whereas the inflection point in the XANES spectrum can be influenced by the shape of the DOS, as discussed below.

The upper curve of Fig. 35 (squares) is our experimental spectrum. The data is better resolved than previously published spectra [61, 58], clearly showing a triple structure, with a shoulder just above the Fermi level, a main peak at 2.4 eV and a smaller peak at 4.1 eV. In the simple scheme discussed above for the electronic structure, the main features of the spectrum correspond to the antibonding bands formed by the Si sp^3 hybrids and the Co d-orbitals.

The middle curve (diamonds) and the lower curve (triangles) are the projected Co d-DOS according to augmented spherical wave (ASW) calculations of van Leuken [70] and the more extended (FLAPW) calculations of Tersoff and Hamann [60], respectively. The theoretical DOS are in both cases convoluted with a gaussian with FWHM of 1.0 eV. This broadening results in an edge slope close to that in the measured spectrum. The broadening is a little larger than would have been expected from the monochromator function (0.7 eV) and the core hole lifetime width (0.32 eV).

The overall shape of the two theoretical spectra is very similar, both reproducing the triple structure confirmed by our measurement. A closer look at the calculated DOS reveals that intensity around the low-energy feature comes from the large DOS-peak, corresponding to the nonbonding orbitals. Both calculations show decreasing intensity of this peak in the region of the Fermi level, and the exact position relative to the Fermi level is then very important for the XANES intensity.

The observation of the low-energy shoulder in the experimental spectrum indicates that the states close to the Fermi level are dominated by nonbonding Co d-type orbitals. Our result puts the 'quasi-gap' between the nonbonding and the antibonding states 1 eV above the Fermi level.

For the falling shape of the DOS one expects a small shift of the inflection point towards lower energies in comparison to a hypothetical step-function DOS. The convolution of the theoretical DOS puts the inflection point at 0.16 eV and 0.14 eV below the Fermi level, for van Leuken and Tersoff and Hamann, respectively. This implies that our data may have to be shifted down with a similar value, and that this value also should be added to our earlier determined $2p_{\frac{3}{2}}$ binding energy.

There are some other minor discrepancies between the experiment and the theory. The ASW calculation overestimates the splitting between the peaks, whereas Tersoff and Hamann accurately predict the peak splitting.

There is also clearly an additional broadening mechanism contributing to the experimental spectrum at higher energies. We attribute this effect to the lifetime broadening due to the excited electron.

When discussing the data at this level of accuracy one has to be aware of the approximations discussed in section 2.2. Especially one could question whether a theory that does not include effects of the core hole could predict the finer details of the spectrum. The fact that the ground state calculations describe all the spectral features with the accuracy demonstrated above would lead us to conclude that the impact on the local DOS of the core hole potential is small. However, Lerch *et al.* [61] claimed to have accounted for core hole effects in their calculation. According to this calculation the inclusion of the core hole does have a large impact on the local d-DOS.

Including more k-points and choosing a larger cell-size for the calculation the core hole effects disappear [66], in agreement with our results and the final state rule.

5.3.3 The Unoccupied Co *d*-DOS of IBS layers

For buried layers the electron yield technique must be replaced by the deep probing fluorescence yield method. FY-SXA measurements are straightforward for dilute and thin samples [47]. The 500 Å thickness of our buried layers is enough to put them in the opposite limit, where the FY signal not directly can be taken as measure of the absorption probability. The FY signal is not proportional to the absorption probability, since the fluorescent photons reach the detector almost independent of the depth at which they originate. This saturation effects have been discussed in section 4.2. Calculating the absorption coefficient from two FY-spectra recorded at different angles using the method presented above, we confirmed that the corrections to the normal incidence spectrum recorded at 89.4° glancing angle are negligible.

In Fig. 36a we show the FY-SXA spectrum, together with the EY data for the $CoSi_2$ single crystal. For intensity reasons we chose to work with a slightly lower resolution , where all the spectral features still can be seen. The concordance between EY and FY spectra again ensures that the FY signal is proportional to absorption. There are, however, some minute differences between the spectra. The low-energy flank gets a little less intensity in the FY than in the EY measurement. The valley between the two peaks is also slightly deeper. We have no conclusive explanation for these differences, though they could be due to surface effects, which are enhanced in EY measurements.

In Fig. 36b we show the EY and FY signals for an ion beam implanted Si wafer sample before annealing. From the position of the peaks we can conclude that the sample is dominated by a $CoSi_2$-similar coordination since more metallic phases would shift the peaks to lower energies. Our result that the as-implanted sample is dominated by $CoSi_2$-similar phases is in agreement with earlier SXE results on similar samples [67], and in line with the conclusions drawn from XPS measurements [65].

We notice, however, that the triple structure expected for crystalline $CoSi_2$ is completely washed-out. As the average Co concentration in the as-implanted state is lower than in stoichiometric $CoSi_2$, we suggest that this is due to small contributions of Co atoms in a local $CoSi_2$-like arrangement in the first coordination shell lacking second shell Co neighbors.

The independence of probing depth, suggested by the similarity of EY and FY spectra, indicates that the as-implanted sample is fairly homogeneous, as far as the local Co electronic structure is concerned.

In Fig. 36c we show the corrected FY spectra for the annealed sample. The spectrum shows a clear single crystal $CoSi_2$ fingerprint, including the low-energy shoulder and the double peak structure. This spectrum indicates that the majority of the Co atoms in the sample are forming $CoSi_2$, and consistant with the results of the L-EXAFS analysis presented in section 4.1 we conclude that the buried layer indeed is crystalline $CoSi_2$.

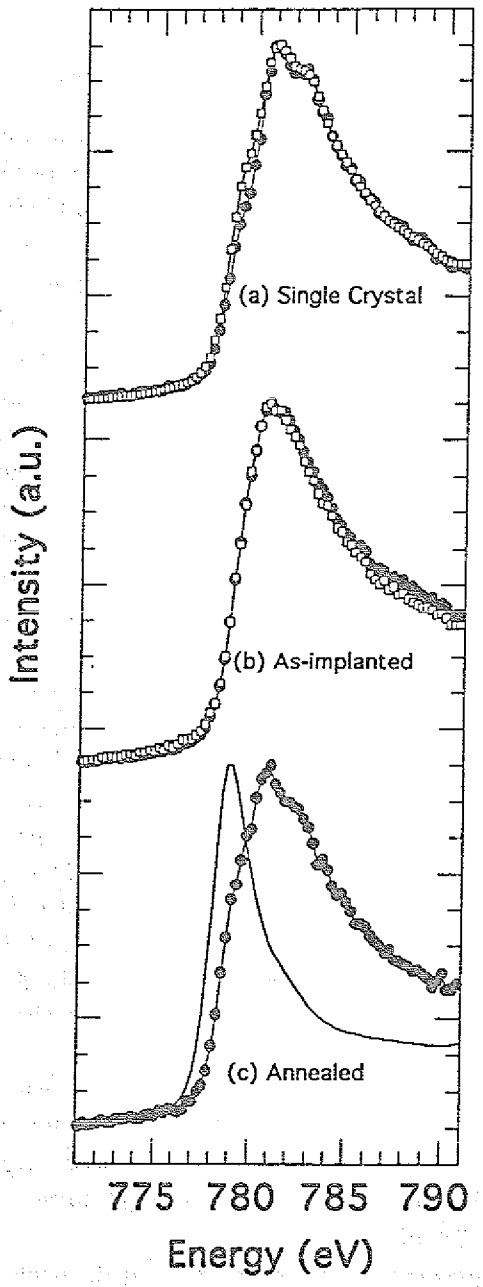

Figure 36: Comparison of total electron yield (empty squares) and fluoresence yield spectra (filled circles), corrected according to eqn. 20, made for (a) the single crystal, (b) an as-implanted Si(111) wafer and (c) an annealed sample. For comparison, EY data for pure Co is included in (c).

5.3.4 The Occupied Co *d*-DOS of $CoSi_2$ and IBS layers

Within our measurement accuracy the Co L_3 SXE spectra of the single crystal and the annealed IBS layer are identical, again demonstrating that the majority of the Co atoms are in the well-defined crystalline $CoSi_2$ phase. The L_3 emission spectrum of $CoSi_2$ is also largely independent of the means of excitation. Following the general discussion of section 5.3.1, we take the SXE spectrum, excited with 3 keV electrons, to represent the occupied Co *d*-DOS (see Fig. 37).

The SXE peak position is 0.3 eV higher than in Co metal. Using the SXE literature value for Co metal, 776.2 eV [68], and our value for the $2p_{\frac{3}{2}}$ binding energy to refer the structures to the Fermi level we find the peak at 2.5 eV binding energy. This value is much higher than estimates from XPS (1.55 eV [65] and 1.9 eV [69]), other SXE measurements (1.6 eV [55]) and from the predictions of band structure calculations (1.6 eV [70] and 1.9 eV [60]). In the light of this evidence we would rather question the L_3 emission literature value for Co metal that we have used for calibration. Since the peak position is used, the determination is dependent on the instrumental resolution. We find that the maximum of a Co L emission spectrum whose width is dominated by the instrumental resolution would be shifted 0.5 eV towards lower energies relative to our metal spectrum.

In Fig. 37 we have chosen to shift our measured *d*-DOS 0.9 eV in the Fermi energy direction, relative to the position determined from our calibration. We again compare to the calculated Co *d*-DOS of van Leuken [70] and Tersoff and Hamann [60], convoluted with 1.0 eV gaussians.

Using the simple scheme for the electronic structure of transition metal silicides we can assign the dominating peak in the spectrum to the nonbonding Co *d*-derived states. The fact that the peak width is substantially smaller (FWHM = 2.4 eV) than the corresponding peak in Co metal (FWHM = 3.3 eV) corroborates the simple picture. Our results disagree on this point with the previously published $CoSi_2$ spectrum [55], which has a width of 3.0 eV, only slightly narrower than Co metal. We believe that the resolving power quoted in Ref. 10 is unattainable using a mica crystal spectrometer at these long wavelengths, and that their spectral width is dominated by instrumental resolution.

Even though our absolute energy scale may be in error we can, via the SXE peak shift (0.3 eV) and the inflection point difference in XANES (0.7 eV), accurately determine that the $CoSi_2$ valence *d*-DOS peak position is shifted 0.4 eV towards higher binding energies, relative to Co metal. In XPS this shift is 0.55 eV [65], although here this shift can be influenced by overlapping intensity from states of other symmetries.

We see that both calculations largely agree on the overall spectral shape, including the narrow peak that corresponds to the nonbonding *d*-orbitals, and the low-energy shoulder that corresponds to the bonding Co 3*d*-Si sp^3 orbitals.

The gaussian convolution gives a theoretical peak width that is smaller than in our measured spectrum. Again, the broadening is clearly higher than expected from the experimental resolution and the core hole lifetime widths, indicating that additional broadening mechanisms are at hand. We believe that the lifetime broadening of the final state mostly contributes to this broadening, but we can also not rule out that correlation effects have an impact on the narrow nonbonding states.

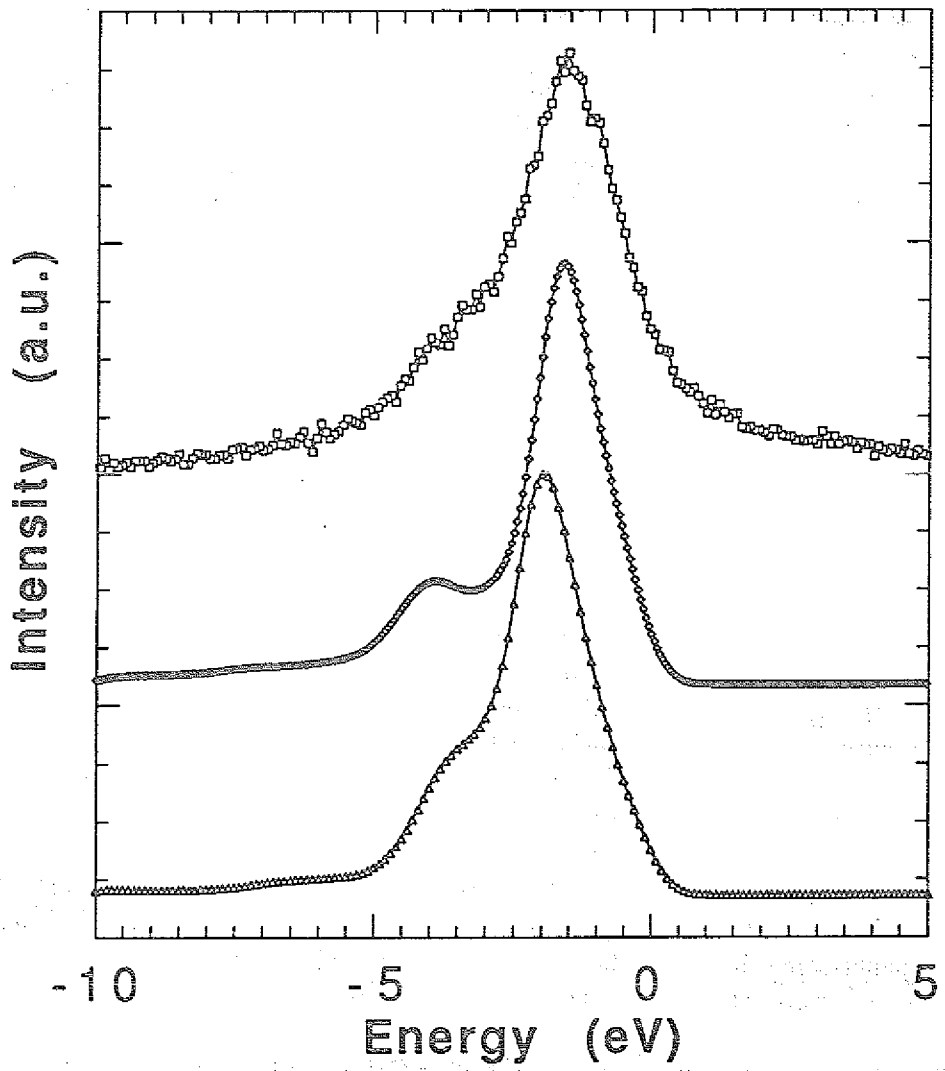

Figure 37: The upper curve (squares) is the Co L_3 emission spectrum of an IBS $CoSi_2$ layer, excited with 3 keV electrons, measured with 0.6 eV resolution, and referred to the Fermi level to compare to the calculations. A shift of 0.9 eV towards the Fermi level was added to the value achieved from the calibration to the SXE spectrum of Co metal, and the binding energy determined by our absorption measurement. The middle curve (diamonds) is the projected Co *d*-DOS according to van Leuken [70] and the lower curve (triangles) according Tersoff and Hamann [60]. Both curves are convoluted with a gaussian of 1.0 eV FWHM.

The shape of the low-energy shoulder is predicted slightly different by the two calculations. The van Leuken calculation is in better agreement with the experimental spectrum. The shoulder is not as clearly separated from the main peak in the calculation of Tersoff and Hamann, resulting in total band width which is too small.

In the vicinity of the Fermi level the identification of spectral features with DOS features is problematic. Here the spectrum can be slightly distorted by double excitation satellites, originating from initial states with an additional valence excitation. (See section 2.2.1.) In correlated systems the extra valence hole acts as a spectator during the transition and shifts the SXE transition towards higher energies [16]. In broad band systems such extra excitations are screened-out during the lifetime of the core hole and no associated satellites are seen. In $CoSi_2$ we expect that the extra excitations from the localized nonbonding states to a large extent are screened out via the broad bonding/antibonding bands. The presence of satellites is suggested in that the cut-off at the Fermi edge is not as sharp as expected for a metallic system. The slow fall-off is, however, also in a satellite-free spectrum expected since the d-DOS decreases with energy in this region.

To estimate the influence of the satellites in our spectrum we show in Fig. 38 the comparison between spectra excited with 3 keV electrons and by the undulator second harmonic radiation from the X1B beamline in Brookhaven. The width of the excitation is around 30 eV situated 20 eV above threshold. This means of excitation should suppress the double excitation satellites [16].

We see a small but clear difference between the two spectra, in the region where the satellites should be expected. The satellite intensity is spread-out over several eV, but does not have a large impact on the spectrum. The only difference, important for the DOS determination, is in the intensity extending above the Fermi level. The steepness of the high-energy side is only slightly different in the more satellite-free photon excited spectrum. The existence of the satellites is a direct indication of correlation: An extra local hole in the nonbonding orbitals is not fully screened-out during the core hole life time.

Apart from the satellites the spectrum from the annealed sample is to a large extent independent of the excitation. For an inhomogeneous sample one one would expect small differences due to the various penetration depths of the excitation agents. The independence of the mode of excitation only demonstrates that the majority of the Co atoms are in the same locally well-defined surrounding.

In Fig. 39 we compare the spectrum of crystalline $CoSi_2$ produced by IBS to the spectrum of a non-annealed as-implanted sample, and find that whereas the position is the same, the width is much larger for the latter system. The spectra are measured with a slightly lower resolution than the spectrum presented in Fig. 37, and we measure the FWHM of the peaks to be 2.6 eV and 3.0 eV.

The smearing-out of the structures can be due to the overlap of emission from atoms at different coordination and consequently different core hole binding energies and local valence electronic structure. We notice however, that the smearing is much more pronounced in SXE than in SXA. This difference is not expected in a multi-phase system, but suggests a single phase where the nonbonding states are more affected by a local distortion than the antibonding states. From the XANES measurement we could rule out that metal richer phases appear in the sample

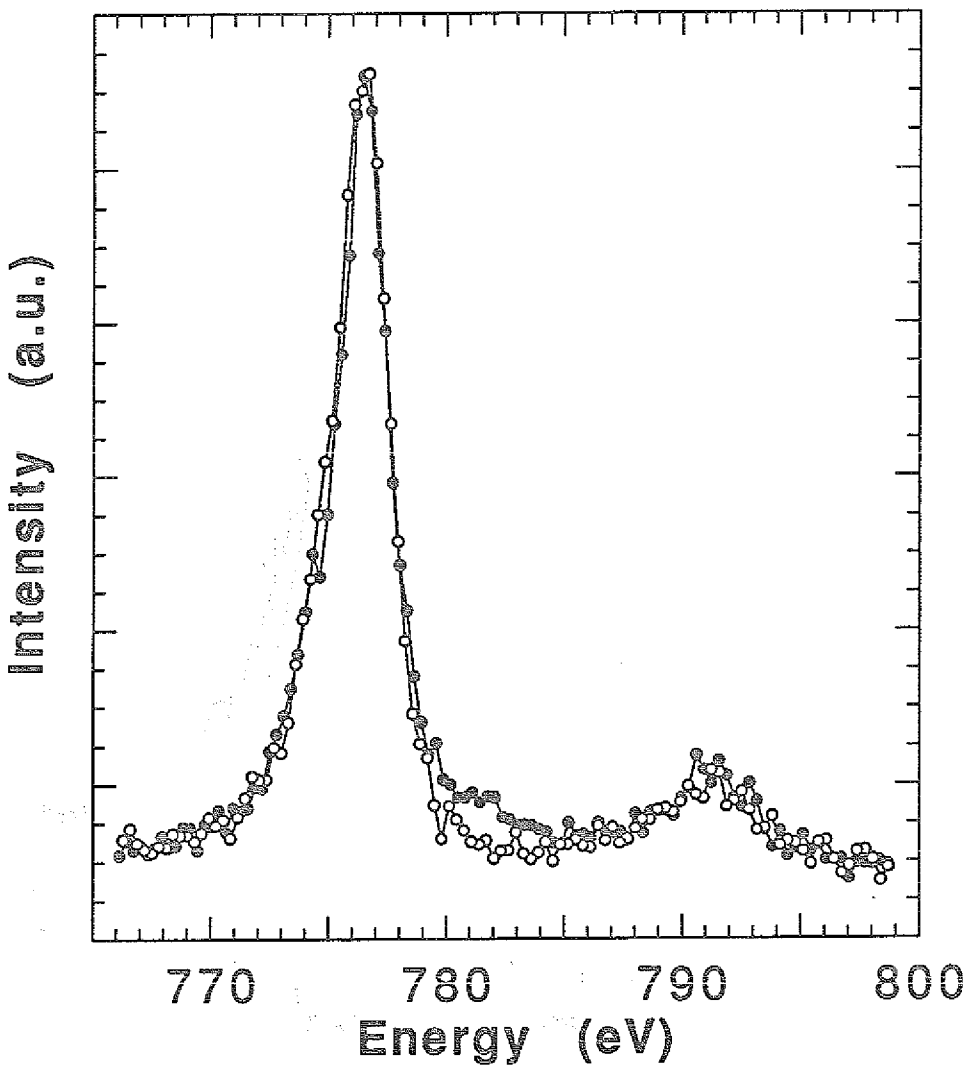

Figure 38: The the Co L_3 emission spectrum of an IBS $CoSi_2$ layer, excited with 3keV electrons (filled circles), and with the second harmonic from the X1 undulator (open circles). The difference above the edge is due to enhanced satellite intensity in the electron excited spectrum. The experimental resolution, being the same for the two spectra, is slightly less than for the spectrum in Fig. 37.

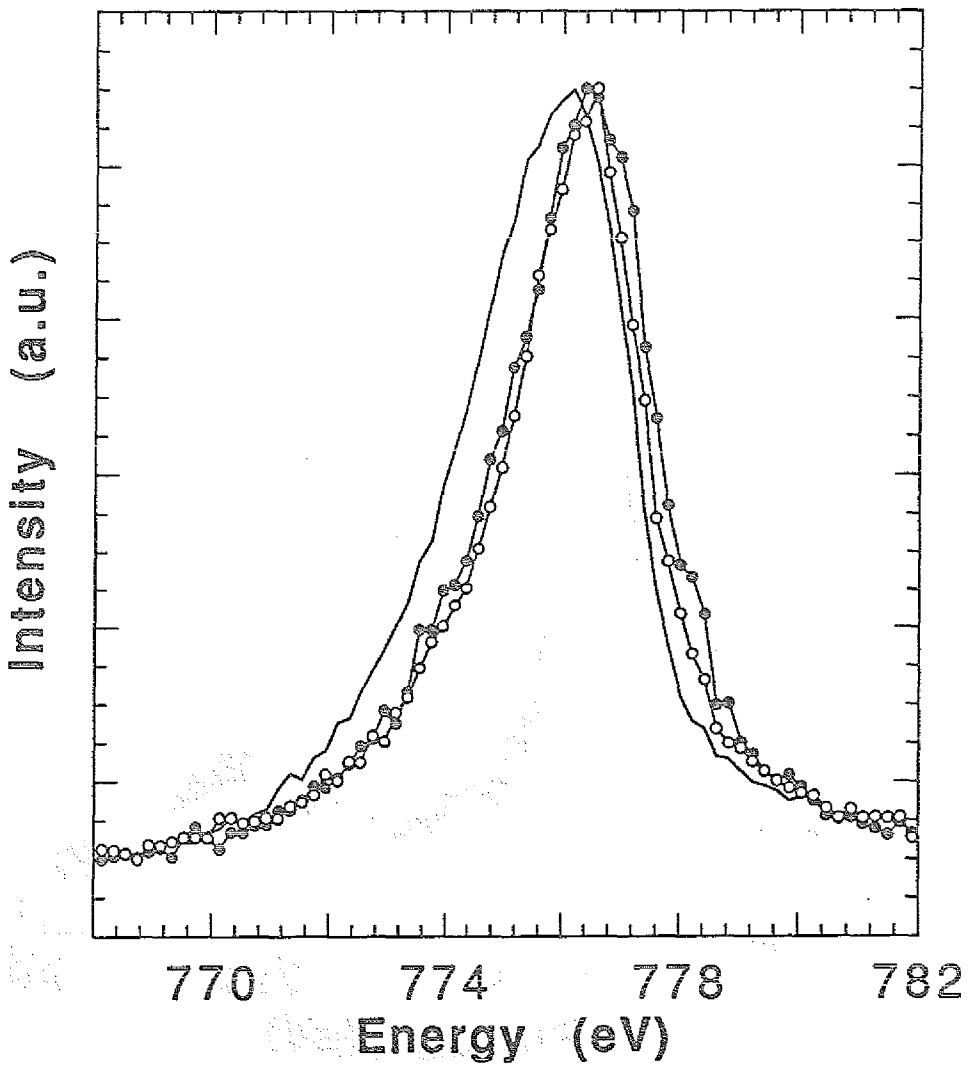

Figure 39: The Co L_3 emission spectrum of an IBS $CoSi_2$ layer (open circles), excited with Cu K fluorescence radiation, compared to a spectrum of the as-implanted sample (filled circles). Also included as a line without markers is the spectrum of Co metal.

to any appreciable extent, and consequently we can rule out that the extra broadening in the SXE spectrum of the as-implanted sample is due to increased metal *d*-*d* overlap. Instead we believe that local symmetry distortions occur around the Co atoms affecting the nonbonding states more than the antibonding states. The symmetry-breaking destroys the nonbonding character of these states, giving an extra broadening due to an overlap with Si orbitals.

5.4 Summary

Using FY-SXA and SXE spectroscopies we have determined the unoccupied and occupied Co *d*-DOS of $CoSi_2$. The measurements were carried out on buried ion-beam synthesized layers, showing that local electronic structure can be determined directly on devices involving layer thicknesses of hundreds of Ångström.

It is shown that electron band calculations correctly predict all the Co *d*-DOS features that we are able to measure. The measurements show that the states in the vicinity of the Fermi level are of nonbonding character, placing the 'quasi-gap' between the nonbonding and the antibonding states 1 eV above the Fermi level. The nonbonding *d*-DOS peak is substantially narrower and shifted towards higher binding energies compared to the *d*-states of pure Co. Correlation is manifested in the appearance of double hole satellites in the SXE spectrum, showing that a local valence hole is not fully screened during the core hole life time.

Our SXE and SXA spectra show that the majority of the Co atoms in the Co ion-implanted Si wafer is in a $CoSi_2$-similar phase, and that upon annealing a buried layer of crystalline $CoSi_2$ indeed is formed.

6 Discussion

In the present work we have studied the electronic and geometric structure of $CoSi_2$ layers embedded in Si wafers. The work had two main directions: the development of methods suited to study buried structures in general and the actual investigation of the $CoSi_2$ layers.

In order to determine the geometric structure of buried silicides, we developed a method to use EXAFS at the $3d$ TM L-edges. We could demonstrate that this new technique is a promising alternative to K-EXAFS for samples in an environment of crystalline Si. The technique was established on a $CoSi_2$ IBS sample and can be used to investigate other silicide layers in future experiments.

Detection of XAS by FY is another technique suited to study buried structures *in situ* due to its deep-probing character and its atomic selectivity. The saturation effects in FY spectra of concentrated samples were analysed. Using the dependence of the FY intensity on the geometry of the experiment, we developed a new method to calculate the absorption coefficient from spectra recorded at different angles. To be able to correct for the saturation effects is of fundamental interest for every user of the FY detection mode, who wants to monitor the x-ray absorption. Even if the saturation effects can be assumed to be negligible due to the nature of the sample or the geometry chosen, the method can be used to check this assumption.

We applied this method in order to investigate the unoccupied electronic states of buried $CoSi_2$ layers by FY-XANES. Additionally, the occupied electronic states of these structures produced by IBS were studied by SXE spectroscopy. As a result, we obtained a complete picture of the Co d-DOS with a resolution that allows for a detailed comparison to theoretical calculations.

By investigating a $CoSi_2$ single crystal in addition to an as-implanted and an annealed IBS sample we gained insight into the evolution of the electronic structure upon silicide formation in the IBS process. We could proove that single crystalline $CoSi_2$ is indeed formed upon annealing. Thus or results are not only of interest with respect to the determination of the electronic structure in $CoSi_2$, but demonstrate that the experimental methods applied can be used for non-destructive investigations of buried layers in microelectronic devices.

References

[1] J.C. Hensel, A.F. Levi, R.T. Tung, and J.M. Gibson, Appl. Phys. Lett. **47**, 151 (1985).

[2] S.P. Murarka in: *Silicides for VLSI Applications* (Academic, New York, 1983).

[3] S. P. Murarka and M.C. Peckerar in: *Electronic Materials, Science and Technology*, p267 (1989).

[4] S. Mantl, Mater. Sci. Rep. **8**, 1 (1992).

[5] A. Schüppen, S. Mantl, L. Vescan, and H. Lüth, Proc. ESSDERC-90 Nottingham, Ed. W. Eccleston and P.J. Rosser p. 45, (Inst. of Physics, London (1990)).

[6] A. E. White, K. T. Short, R. C. Dynes, J. P. Gasno and J. M. Gibson, Appl. Phys. Lett.**50**, 95 (1987).

[7] R. Jebasinski, S. Mantl, L. Vescan, and Ch. Dieker, Appl. Surf. Sci. **53**, 264 (1991).

[8] S. Eisebitt, T. Böske, J.-E. Rubensson, R. Jebasinski, S. Mantl, J. Kojnok, P. Skytt, J.-H. Guo, N. Wassdahl, J. Nordgren, K. Holldack, and W. Eberhardt, submitted to Phys. Rev. B.

[9] S. Eisebitt, T. Böske, J-E. Rubensson and W. Eberhardt, submitted to Phys. Rev. B.

[10] J.E. Rubensson: *Electronic structure determined by soft x-ray emission spectroscopy* in: 23. IFF Ferienkurs, Forschungszentrum Jülich (1992).

[11] D.A. Goodings and R. Harris, J. Phys. C, Ser.2 **2** 1808 (1969).

[12] T. Jarlborg and P.O. Nilsson, J. Phys. C, **12** 265 (1978).

[13] J.E. Müller and J.W. Willkins, Phys. Rev. B **29**, 4331 (1984).

[14] U. von Barth and G. Grossman, Phys. Rev. B **25**, 5150 (1982).

[15] 23. IFF Ferienkurs des Forschungszentrums Jülich *Synchrotronstrahlung zur Erforschung kondensierter Materie* (1992).

[16] N. Wassdahl, J-E. Rubensson, G. Bray, P. Glans, P. Bleckert, R. Nyholm, S. Cramm, N. Mårtensson, and J. Nordgren, Phys. Rev. Lett. **64**, 2807 (1990).

[17] G.D. Mahan, Phys. Rev. **153**, 882 (1967).

[18] P. Nozières and C.T. de Dominicis Phys. Rev. **178**, 1097 (1969).

[19] E. Zaremba and K. Sturm, Phys. Rev. Lett. **66**, 2144 (1991).

[20] B. Lengeler: *Röntgenabsorptionsspektroskopie* in: 23. IFF Ferienkurs, Forschungszentrum Jülich (1992).

[21] E.A. Stern in: *X-Ray Absorption: Principles, Applications, Techniques of EXAFS, SEXAFS and XANES*, ed. D.C. Konigsberger and R. Prins, Chemical Analysis Vol 92 (Wiley-Intersience, New York, 1988)

[22] B.K. Teo *EXAFS: Basic Principles and Data Analysis*, Inorganic chemistry concepts Vol. 9 (Springer, Berlin, 1986)

[23] P.A. Lee, P.H. Citrin, P. Eisenberger, and B.M. Kincaid, Rev. Mod. Phys. **53**, 769 (1981).

[24] B.K. Teo and P.A. Lee, J. Am. Chem. Soc. **101**, 2815 (1979).

[25] M. Domke, T. Mandel, A. Puschmann, C. Xue, D.A. Shirley, G. Kaindl, H. Petersen, and P. Kuske, Rev. Sci. Instr. **63**, 80 (1992).

[26] H. Peterson, Nucl. Instr. Meth. Phys. Res. A **246**, 260 (1986).

[27] J. Nordgren, G. Bray, S. Cramm, R. Nyholm, J-E. Rubensson and N. Wassdahl, Rev. Sci. Instr. **60**, 1690 (1989).

[28] K, Randall, J. Feldhaus, A.M. Bradshaw, W. Eberhardt, Y. Ma, and P.D. Johnson, Rev. Sci. Instr. **63**, 1367 (1992).

[29] J. Kojnok, A. Szasz, W. Krasser, G. Marks, V.S. Stepanjuk, and A.A. Katsnelson, J. Phys.: Cond. Matt. **4**, 2487 (1992);

[30] I.A. Britov, E.A. Obolenskii, M.S. Goldengerg, L.G. Rabinovich, and T.M. Antoeva, Prib. Tekh. Eksp. **1**, 288 (1983).

[31] S.M. Heald, E. Keller, and E.A. Stern Phys. Lett. **103A**, 155 (1984).

[32] Z. Tan, F. Namavar, J.I. Budnick, F.H. Sanchez A. Fasihuddin, S.M. Heald, C.E. Bouldin, and J.C. Woicik, Phys. Rev B **46**, 4077 (1992).

[33] D. Denley, R.S. Williams, P. Perfetti, and D.A.Shirley, Phys. Rev. B **19**, 1762 (1979).

[34] Pearson's Handbook of Crystallographic Data for Intermetallic Phases, Vol. 1, edited by P. Villars and L.D. Calvert, American Society for Metals, p. 1830 (1985).

[35] H. Meyerheim, Ph.D. thesis, FU Berlin (1990).

[36] L. Tröger, D. Arvanitis, K. Baberschke, H. Michaelis, U. Grimm, and E. Zschech, Phys. Rev. B **46**, 3283 (1992).

[37] J.J. Yeh and I. Lindau, Atomic Data and Nuclear Data Tables **32**, 47 (1985).

[38] W.J. Veigele in: *Handbook of Spectroscopy* Vol.1, Ed. J.W. Robinson, CRC Press, Cleveland (1974).

[39] J. C. Fuggle and N. Mårtensson, J. Electron Spec. **21**, 275 (1980)

[40] B. Lengeler and P. Eisenberger, Phys. Rev B **21**, 4507 (1980).

[41] Z. Tan, J.I. Budnick, F.H. Sanchez, G. Tourillon, F. Namavar, and H.C. Hayden, Phys. Rev. B **40**, 6368 (1989).

[42] Eds.: M. Cardona and L. Ley, *Photoemission in Solids I: General Principles*, Springer Berlin (1978).

[43] P.A. Lee and J.B. Pendry, Phys. Rev. B **11**, 2795 (1975).

[44] S.J. Gurman, N. Binsted, and I. Ross, J. Phys. C **17**, 143 (1984).

[45] S.J. Gurman, N. Binsted, and I. Ross, J. Phys. C **19**, 1845 (1986).

[46] A. Krol, C.S. Lin, Z.H. Ming, C.J. Sher, Y.H. Kao, C.T. Chen, F. Sette, Y. Ma, G.C. Smith, Y.Z. Zhu, and D.T. Shaw, Phys. Rev. B **42**, 2635 (1990).

[47] J. Jaklevic, J.A. Kirby, M.P. Klein, A.S. Robertson, G.S. Brown, and P. Eisenberger, Solid State Comm. **23**, 679 (1977).

[48] E. Zschech, L. Tröger, D. Arvanitis, H. Michaelis, U. Grimm, and K. Baberschke, Solid State Comm. **82** , 1 (1992).

[49] D.M. Pease, D.L. Brewe, Z. Tan, and J.I. Budnick, Phys. Lett. A **138** , 230 (1989).

[50] L.Tröger, D.Arvanitis, K. Baberschke, H. Michaelis, U. Grimm, and K.Baberschke, Phys. Rev. B **41**, 7297 (1990).

[51] B.L. Henke, P. Lee, T.J. Tanaka, R.L. Shimabukuro, and B.K. Fujikawa in: Atomic Data and Nuclear Data Tables **27**, 1 (1982).

[52] H. Nakamura, M. Iwami. M. Hirai, M. Kusaka, F. Akao, and H. Watabe, Phys. Rev. B **41**, 12042 (1990).

[53] J.J. Jia, T.A. Callcott, W.L. O'Brien, Q.Y. Dong, J.-E. Rubensson, D.R. Mueller, D.L. Ederer, and J.E. Rowe, Phys. Rev. B **43**, 4863 (1991).

[54] P.J.W. Weijs, E. van Leuken, R.A. de Groot, J. C. Fuggle, S. Reiter, G. Wiech, and K.H.J. Buschow, Phys. Rev. B **44**, 8195 (1991).

[55] E. Belin, C. Senemaud, L. Marinage, J.Y Veuillen, D.A. Papaconstantopoulos, A. Pasture, and F. Cyrot- Lackmann, J. Phys.: Condens. Matter **2**, 3247 (1990).

[56] G.W. Rubloff, Surf. Sci. **132**, 268 (1983).

[57] P.J.W. Weijs, G. Wiech, W. Zahorowski, W. Speier, J.B. Goedkoop, M. Czyzyk, J.F. Acker, E. van Leuken, R.A. de Groot, G. van der Laan, D.D. Sarma, L. Kumar, K.H.J. Buschow, and J.C. Fuggle, Phys. Scripta **41**, 629 (1990)

[58] W. Speier, thesis, KFA Jülich, internal publication Jül-2819 (1988).

[59] C. Calandra, O. Bisi, and G. Ottaviani, Surf. Sci. Rep. 4, 271 (1984).

[60] J. Tersoff and D.R. Hamann, Phys. Rev. B **28**, 1168 (1983).

[61] P. Lerch, T. Jarlborg, V. Codazzi, G. Loupias, and A.M. Flank, Phys. Rev. B **45**, 11481 (1992).

[62] R. Nyholm, N. Mårtensson, A. Lebugle, and U. Axelsson, J. Phys. F: Metal Phys. **11**, 1727 (1981).

[63] B.T. Thole, R.D. Cowan, G.A. Sawatzky, J. Fink, and J.C. Fuggle, Phys. Rev. B **31**, 6856 (1985).

[64] J. Fink, Th. Müller-Heinzerling, B. Scheerer, W. Speier, F.U. Hillebrecht, J.C. Fuggle, J. Zaanen, and G.A. Sawatzky, Phys. Rev. B **32**, 4899 (1985).

[65] V. Kinsinger, I. Dózsi, P. Steiner, and G. Langouche, J. Phys. F: Met. Phys. **18**, 1515 (1988).

[66] P. Lerch, private communication.

[67] J. J. Jia, T. A. Callcott, W. L. O'Brien, Q. Y. Dong, D. R. Mueller, J-E. Rubensson, D. L. Ederer, Z. Tan, F. Namavar and J. I. Budnick, J. Appl. Phys., 69, 7800 (1991).

[68] J.A. Bearden, Rev. Mod. Phys. **39**, 78 (1967).

[69] C. Pirri, J.C. Peruchetti, G. Gewinner, and J. Derrien, Phys. Rev. B **29**, 3391 (1984).

[70] E. van Leuken, thesis, Katholieke Universiteit Nijmegen (1986)

Acknowledgements

This diploma thesis has been written at the *Institut für Elektronische Eigenschaften* (IEE) within the *Institut für Festkörperforschung* of the *Forschungszentrum Jülich* (KFA).
First and foremost I would like to thank the whole IEE team. It was a pleasure to work in this group due to the friendly and constructive atmosphere of real teamworking.

I am greatly indebted to Wolfgang Eberhardt who stimulated and supported this work. He was always present for inspiring discussions.

I thank Jan-Eric Rubensson for introducing me into the world of SXE and SXA. I learned a lot of physics from him in a very pleasant way. Working with him was fun.

I would like to thank Thomas Böske for many discussions and the cooperation on the various experiments in long synchrotron beamline nights.

This work would not have been possible without Rolf Jebasinski and S. Mantl from the *Institut für Schicht- und Ionentechnik* in the KFA. They produced and kindly supplied the buried $CoSi_2$ layers. I enjoyed this fruitful cooperation.

Special thanks to Stefan Cramm for his advices concerning EXAFS and XPS and his help on any possible computer problem.

I thank Joseph Kojnok for his measurements with the crystal spectrometer in Budapest and for many discussions.

Thanks to Karsten Holldack for his help with the fluorescence chamber and to M. Domke and G. Remmers for their assistance at the SX-700-2/BESSY.

I would like to thank everyone involved in the measurements at X1B/NSLS: P. Skytt, J.-H. Guo, N. Wassdahl, Y. Ma, and P.D. Johnson. Special thanks to Joseph Nordgren for the possibiliy to use the 'Uppsala spectrometer'.

I thank Claus Malten for many discussions and for helping out at the XPS system.

I would like to thank Uwe Döbler for kindly providing the $CoSi_2$ single crystal.

Special thanks to Jutta Gollnick for all her help with any bureaucracy and for her great contributions to the friendly atmposphere in our group.

FORSCHUNGSZENTRUM JÜLICH GmbH

KFA

Jül-2715
January 1993
ISSN 0366-0885